Cerebellar defects in *Pdss2* conditional knockout mice during embryonic development and in adulthood

Song Lu[a], Lin-Yu Lu[a,1], Meng-fei Liu[a], Qiu-Ju Yuan[a,2], Mai-Har Sham[a], Xin-Yuan Guan[b], Jian-Dong Huang[a,*]

Author affiliations:

[a]Department of Biochemistry, University of Hong Kong, Faculty of Medicine Building, Pokfulam, Hong Kong SAR, China

[b]Department of Clinical Oncology, University of Hong Kong, Faculty of Medicine Building, Pokfulam, Hong Kong SAR, China

*Corresponding author. Tel.: +852 2819 2810; Fax: +852 2855 1254. *E-mail address*: jdhuang@hkucc.hku.hk (J.D. Huang)

[1]Present address: Division of Molecular Medicine and Genetics, Department of Internal Medicine, University of Michigan Medical School, 5552 MSRB II, 1150 W. Medical Center Drive, Ann Arbor, Michigan, 48109, USA

[2]Present address: Department of Anatomy, University of Hong Kong, Faculty of Medicine Building, Pokfulam, Hong Kong SAR, China

Abbreviations: ETS, electron transport system; ROS, reactive oxygen species; TCA, tricarboxylic acid; MPT, mitochondrial permeability transition; PHB,

para-hydroxybenzoate; PDS, *trans*-prenyl diphosphate synthase; BAC, bacterial artificial chromosome.

Abstract

PDSS2 is a gene that encodes one of the two subunits of *trans*-prenyl diphosphate synthase that is essential for ubiquinone biosynthesis. It is known that mutations in *PDSS2* can cause primary ubiquinone deficiency in human and a similar disease in mouse. Cerebellum is the most often affected organ in ubiquinone deficiency, and cerebellar atrophy has been diagnosed in many infants with this disease. In this study, two *Pdss2* conditional knockout mouse lines directed by *Pax2-cre* and *Pcp2-cre* were generated to investigate the effect of ubiquinone deficiency on cerebellum during embryonic development and in adulthood, respectively. The *Pdss2*$^{f/-}$*; Pax2-cre* mouse recapitulates some symptoms of ubiquinone deficiency in infants, including severe cerebellum hypoplasia and lipid accumulation in skeletal muscles at birth. During early cerebellum development (E12.5-14.5), *Pdss2* knockout initially causes the delay of radial glial cell growth and neuron progenitor migration, so the growth of mutant cerebellum is retarded. During later development (E15.5-P0), increased ectopic apoptosis of neuroblasts and impaired cell proliferation result in the progression of cerebellum hypoplasia in the mutant. Thus, the mutant cerebellum contains fewer neurons at birth, and the cells are disorganized. The developmental defect of mutant cerebellum does not result from reduced *Fgf8* expression before E12.5. Electron microscopy reveals mitochondrial defects and increased autophagic-like vacuolization that may arise in response to abnormal mitochondria in the mutant cerebellum. Nevertheless, the mutant mice die soon after birth probably due to cleft palate and micrognathia, which may result from *Pdss2* knockout caused by ectopic *Pax2-cre*

expression in the first branchial arch. On the other hand, the *Pdss2*$^{f/-}$*; Pcp2-cre* mouse is healthy at birth but gradually loses cerebellar Purkinje cells and develops ataxia-like symptoms at 9.5 months; thus this conditional knockout mouse may serve as a model for ubiquinone deficiency in adult patients. In conclusion, this study provides two mouse models of *Pdss2* based ubiquinone deficiency. During cerebellum development, *Pdss2* knockout results in severe cerebellum hypoplasia by impairing cell migration and eliciting ectopic apoptosis, whereas *Pdss2* knockout in Purkinje cells at postnatal stages leads to the development of cerebellar ataxia.

Key words:

PDSS2, ubiquinone deficiency, cerebellum development, apoptosis, cell migration, Purkinje cell, ataxia

Introduction

Ubiquinone (coenzyme Q) is an important lipid soluble electron carrier in the mitochondrial respiratory chain, in which it transports electrons from Complex I or Complex II to Complex III. As a well-known antioxidant, ubiquinone prevents cells from reactive oxygen species (ROS) damage by scavenging free radicals. Besides, it is also involved in the modulation of thermogenesis and mitochondrial permeability transition (MPT) (Klingenberg and Echtay, 2001; Walter et al., 2000). Primary ubiquinone deficiency is a rare heterogeneous genetic disorder in human. There are five subtypes of ubiquinone deficiency according to different clinical symptoms, and skeletal muscle, cerebellum, and kidney are often affected (Quinzii et al., 2007a; Quinzii et al., 2007b). Although this disease is usually treated by prolonged CoQ_{10} therapy, not all patients demonstrate substantial improvement, especially for those who have already developed severe lesions in central nerve system (CNS) or kidney (Rotig et al., 2000; Salviati et al., 2005).

Mammals can acquire ubiquinone either from diet or by *de novo* synthesis. However, since the intestinal ubiquinone uptake is usually inefficient, human body largely relies on endogenous ubiquinone under normal circumstance (Turunen et al., 2004). Consequently, any genetic defect in ubiquinone biosynthesis or metabolism will result in primary ubiquinone deficiency. Ubiquinone is composed of a modified quinonoid ring derived from *para*-hydroxybenzoate (PHB) and a polyprenyl side chain with varied numbers of isoprene subunits. In animals, PHB is derived from

tyrosine or phenylalanine, and isoprene is synthesized from acetyl CoA through mevalonate pathway (Meganathan, 2001; Quinzii et al., 2007b). The long isoprenyl side chain is essential to maintain the molecule's hydrophobicity, which enables ubiquinone to perform important biological functions in various cell membranes. One crucial enzyme for the condensation of polyprenyl side chain is *trans*-prenyl diphosphate synthase (PDS), which also determines the predominant side chain length of ubiquinone in a given species (Turunen et al., 2004). In human and mouse, PDS is a heterotetramer consisting of two PDSS1 subunits and two PDSS2 subunits, and both of them are indespensible for PDS enzymatic activity (Saiki et al., 2005).

As PDS is the enzyme at the first committed step in ubiquinone synthesis, mutations in either *PDSS1* or *PDSS2* gene can result in primary ubiquinone deficiency in human (Lopez et al., 2006; Mollet et al., 2007). Interestingly, a mouse strain (*kd/kd*) harboring a spontaneous mis-sense mutation in *Pdss2* gene also develops a progressive kidney disease similar to that observed in ubiquinone deficient patients with defective *PDSS2* gene (Peng et al., 2008). At about 8 weeks old, the *kd/kd* mouse develops kidney symptoms reminiscent of human juvenile collapsing glomerulopathy, and it gradually progresses to end stage renal disease at 16-40 weeks (Peng et al., 2004). Further characterization of this mutant mouse has revealed that kidney podocytes, which are selectively affected, undergo de-differentiation and overlay the collapsed capillary loops (Barisoni et al., 2005). Moreover, CoQ_{10} supplementation can also alleviate the renal symptoms of *kd/kd* mouse to some extent (Saiki et al., 2008). Thus, this mutant mouse can be utilized to study the kideny symptoms of

human ubiquinone deficiency, but other organs commonly involved in the disease are not affected. Therefore, a more sophisticated tissue specific *Pdss2* knockout mouse model will be valuable to elucidate the pathogenesis of ubiquinone deficiency in different organs.

The mouse homologous gene of human *PDSS2*, *Pdss2*, is located on chromosome 10 (10q B2). Both mouse *Pdss2* and human *PDSS2* contain eight exons, and there are at least two mRNA variants arising from alternative splicing, but it is believed that the longer form including all eight exons is fully functional (Lopez et al., 2006; Saiki et al., 2005). Human and mouse PDSS2 proteins are also very similar in that they both consist of seven conserved domains. In the *kd/kd* mutant mouse, the renal disease is considered to be associated with a point mutation in exon 2 of *Pdss2*, which leads to an amino acid substitution (V117M) in the first conserved domain (Peng et al., 2004; Saiki et al., 2005), suggesting the important function of this region in PDSS2 protein. Previously, we generated a *Pdss2* floxed mouse ($Pdss2^{f/f}$) with exon 2 flanked by two LoxP sites. However, with the deletion of *Pdss2* exon 2, the total knockout mouse ($Pdss2^{-/-}$) is embryonic lethal, which is consistent with the hypothesis that ubiquinone is essential for mouse embryonic development (Levavasseur et al., 2001). Consequently, a tissue specific knockout strategy has to be adopted.

Tissue specificity is a prominent feature of ubiquinone deficency. In addition to kidney, cerebellum is one of the most often affected organs in ubiquinone deficiency, as it is involved in four out of five subtypes of this disease (Rotig et al., 2007).

Meanwhile, a considerable portion of genetically undefined cerebellar ataxia is associated with ubiquinone deficiency (Lamperti et al., 2003). Because of its limited capacity of repair, cerebellum is more vulnerable than skeletal muscles, as patients with cerebellar atrophy cannot fully recover after CoQ_{10} therapy (Lalani et al., 2005; Ogasahara et al., 1989). Furthermore, in some cases of ubiquinone deficiency, cerebellar atrophy may develop very early in life, even at infantile stage (Lopez et al., 2006; Musumeci et al., 2001). Thus, it is possible that cerebellum has already been affected during embryonic development. However, the pathogenesis of cerebellum defect in ubiquinone deficient patients has not been thoroughly investigated due to limited clinical samples, and there has not been any mouse model established so far to address this issue. Therefore, the main objective of this study is to analyze the cerebellum defect in ubiquinone deficiency with the emphasis on cerebellum development using a *Pdss2* conditional knockout mouse model. In order to achieve *Pdss2* knockout in developing cerebellum, the previously generated *Pdss2* floxed mouse (*Pdss2*$^{f/f}$) was crossed with a *Pax2-cre* deleter mouse, in which Cre recombinase is expressed in the hindbrain region at E9.5 and influences many cells in cerebellum at birth (Ohyama and Groves, 2004). At the same time, a more specific deleter mouse *Pcp2-cre* (Zhang et al., 2004) was also crossed with *Pdss2*$^{f/f}$ mouse to generate another tissue specific knockout mouse (*Pdss2*$^{f/-}$*; Pcp2-cre*), where *Pdss2* knockout occurs only in cerebellum Purkinje cells after birth. This latter conditional knockout mouse can be used to study the cerebellar defects of ubiquinone deficiency in adulthood.

In this study, two *Pdss2* conditional knockout mice (*Pdss2*$^{f/-}$*; Pax2-cre* and *Pdss2*$^{f/-}$*; Pcp2-cre*) were generated. The phenotypes of *Pdss2*$^{f/-}$*; Pax2-cre* mouse were characterized at birth with respect to human ubiquinone deficiency, and the cerebellum development was also studied at different embryonic stages. Besides, the cerebellum of *Pdss2*$^{f/-}$*; Pcp2-cre* mouse was briefly studied at different ages in adulthood.

Materials and methods

Mouse breeding and colony maintenance

All mice used in this study were maintained on a common C57BL/6N (C57) genetic background at the minimum disease area of the Laboratory Animal Unit in the University of Hong Kong, and the experimental protocols were approved by the Committee on the Use of Live Animals in Teaching and Research (CULATR). Mice were marked by ear puncture, and DNA was extracted from ear clips as described before (Wu et al., 2008). Mouse genomic DNA (50-100 ng) was used as template for one routine PCR genotyping. The genotyping primers and amplification conditions are summarized in Table 1, and typical results shown in Fig. 1A. For timed mating, the day when vaginal copulation plug was observed was considered as E0.5, and the desired embryonic stage was counted accordingly.

The breeding strategy to generate tissue specific knockout mouse from the founder is illustrated in *Supplementary data* (Fig. S3), and different *Pdss2* alleles involved are demonstrated in Fig. 1A. Briefly, the founder mouse (*Pdss2*$^{f\text{-}E\text{-}Neo/+}$) was crossed to *β*-actin-cre (Lewandoski et al., 1997) for heterozygous knockout mouse (*Pdss2*$^{+/-}$) and to FLPeR (Farley et al., 2000) for heterozygous floxed mouse (*Pdss2*$^{f/+}$). Then, *Pdss2*$^{+/-}$ mouse was bred with tissue specific deleter mouse *Pax2-cre* (Ohyama and Groves, 2004) or *Pcp2-cre* (Zhang et al., 2004) to produce the compound mutant mouse *Pdss2*$^{+/-}$*; Pax2-cre* or *Pdss2+/-; Pcp2-cre*. Meanwhile, the homozygous floxed mouse (*Pdss2*$^{f/f}$) was obtained by intercrossing *Pdss2*$^{f/+}$ mice. In

order to demonstrate the *Pax2-cre* and *Pcp2-cre* expression pattern, *ROSA26*^{lacZ} reporter gene was introduced by crossing *Pdss2*$^{f/f}$ mouse with *ROSA26*$^{laZ/lacZ}$ mouse (Soriano, 1999). Finally, *Pdss2*$^{+/-}$*; Pax2-cre* or *Pdss2*$^{+/-}$*; Pcp2-cre* male mice were crossed to either *Pdss2*$^{f/f}$ or *Pdss2*$^{f/f}$*; ROSA26*$^{laZ/lacZ}$ female mice from the same generation to produce desired tissue specific knockout mice (*Pdss2*$^{f/-}$*; Pax2-cre* or *Pdss2*$^{f/-}$*; ROSA26*$^{laZ/+}$*; Pax2-cre* and *Pdss2*$^{f/-}$*; Pcp2-cre* or *Pdss2*$^{f/-}$*; ROSA26*$^{laZ/+}$*; Pcp2-cre*). In most experiments, progenies from the same dame were used.

RNA extraction and RT-PCR

Total RNA was extracted from mouse kidney using Trizol reagent (Invitrogen) following the manufacturer's instruction. Reverse transcription was performed using 1-3 μg total RNA as template with Moloney Murine Leukemia Virus (M-MLV) reverse transcriptase (Promega) according to the instruction. Subsequently, the fragment of *Pdss2* exon 1 to part of exon 5 was amplified from cDNA by RT-f1 (5'-ATGAGCCTCCGGCAGCTGCTG-3') & RT-r5 (5'-CTGGCAGCTCTTCGCTAGCA-3'). The desired PCR products were purified and sequenced using *Pdss2*-Ex3-seq-r1 (5'-AGAAAGTCTCCACTCAGGATAGCT-3').

Western blot

Protein from freshly isolated mouse tissue was extracted with 50-200 μL RIPA buffer (50 mM Tris·HCl (pH7.5), 150 mM NaCl, 0.5% sodium dexoycholate, 1% NP-40) supplemented with 0.05 mM PMSF and complete protease inhibitor cocktail

(Roche). For each sample, 10-20 μg protein was resolved by 12% SDS-PAGE and transferred to a PVDF membrane (Hybond^{TM}-C super membrane, Amersham Bioscience). The membrane was blotted with a mouse monoclonal antibody against PDSS2 (1:2,000, Wolwo Biotech) (Fung et al., 2009) and a mouse monoclonal antibody against α-tubulin (1:10,000, Sigma). The size of PDSS2 and α-tubulin was detected as 37 KDa and 55 KDa, respectively.

Whole mount in situ hybridization and histochemistry

Embryos at E10.5 and E11.5 were collected for whole mount *in situ* hybridization following the protocol described previously (Wilkinson, 1992) with modifications described below. The embryos were treated by 10 μg/mL proteinase K (Roche) in PBST at RT: 50 min for E10.5 and 90 min for E11.5. For final color development, the embryo was incubated with BM purple solution (Roche) at RT until satisfactory color achieved. The plasmid of *Fgf8* probe was generously provided by Prof. K. SE. Cheah (Crossley and Martin, 1995). It was linearized with *Bam*H I and used as template to synthesize a DIG labeled RNA probe (about 850 bp) by *in vitro* transcription (DIG RNA labeling kit, Roche). The final concentration of labeled probe was 0.1-0.2 ng/μL for whole mount *in situ* hybridization.

Whole mount skeleton staining with Alcian blue & Alizarin red S was performed according to the procedure described before (Kimmel and Trammell, 1981; McLeod, 1980). Whole mount X-gal staining was conducted as described previously (Zhang et al., 2004). Embryos younger than E12.5 were directly stained. For older embryos and

postnatal mice, tissues of interest were first isolated and then stained separately.

Histology and immunohistochemistry

For routine paraffin section, mouse tissues or embryos were fixed in 10% neutral buffered formalin at 4℃ overnight and dehydrated through ethanol series. The tissues were embedded with proper orientation in paraffin and sectioned at 5-7 μm thickness (Microm-HM340E, Leica). For frozen section, tissues were fixed in 10% neutral buffered formalin at 4℃ for 3-4 hr and infiltrated with 30% sucrose (in PBS) at 4℃ overnight. Tissues were embedded with OCT compound (Leica Microsystems) and frozen in isopentane cooled by liquid nitrogen. Then the tissue blocks were archived at -80℃ and sectioned at 7-10 μm (CM 1900UV, Leica). Routine H&E staining and Sudan black staining for lipid were performed following the protocols described previously (Carson, 1990).

For immunostaining, the primary antibodies were applied as followed: mouse anti-CALB-28K (Sigma) at 1:100, rabbit anti-β-galactosidase (Cappel-INC, MP Biomedicals) at 1:400, mouse anti-nestin (BD Pharmigen) at 1:2,000, and mouse anti-TUJ1 (Convance) at 1:500. HRP conjugated goat anti-rabbit or anti-mouse IgG antibody (Dako cytomation, Envision + system) was used for immunohistochemistry, and color was developed by DAB (Dako). For immunofluorescence, Cy3 labeled goat anti-rabbit IgG (1:5,000, Jackson ImmunoResearch Laboratories) was applied, and section was mounted with anti-fade reagent containing DAPI (Invitrogene).

Cell proliferation and apoptosis assay

Cell proliferation in mouse embryo was studied by BrdU incorporation assay. BrdU stock solution (5 mg/mL, Sigma) was administered to pregnant mice via intra-peritoneal injection (50 μg BrdU per gram body weight) 2 hr prior to euthanization. The embryos were processed for paraffin section as usual. Brain sections were pre-treated with trypsin at 37℃ for 5-7 min, and BrdU detection was performed using BrdU staining kit (Zymed, Invitrogen) according to the instruction.

Apoptosis was examined by TUNEL assay using *in situ* cell death detection kit (Roche) with the following modifications. Paraffin sections of newborn mouse brain or embryos were pre-treated with permeabilizing solution (0.1% Triton X-100, 0.1% sodium citrate) for 7 min at RT, whereas adult mouse brain samples were digested by 25 μg/mL proteinase K (Roche) for 30 min at 37℃. For immunohistochemistry, the concentration of convertor-POD solution was reduced to 1/3 (diluted with TBS) to lessen the background.

Electron microscopy

Cerebellum was retrieved from adult mice or embryos and cut into small blocks. They were fixed with 2.5% glutaraldehyde (in 0.1 M cacodylate buffer) at 4℃for 4 hr, washed, and infiltrated with 0.1 M sucrose at 4℃ overnight. After three washes with 0.1 M cacodylate buffer, the tissues were post-fixed in 1% OsO_4 at RT for 1 hr. Then, the tissues were dehydrated through ethanol series, infiltrated with epoxy resin, and

embedded at proper orientation. Sections were cut by ultramicrotom (Leica Ultracut UCT) and examined by transmission electron microscope (Philips EM208s) at the Electron Microscope Unit of the University of Hong Kong.

Foot print assay

Four mutant (*Pdss2*$^{f/-}$*; Pcp2-cre*) mice and their control littermates (*Pdss2*$^{f/+}$*; Pcp2-cre*) were evaluated by foot printing assay following the same method as described previously (Gerfen et al., 2007). Results from 5 days (at least 3 repetitive walking tasks for each mouse on each day) were analyzed. The stride length between two consecutive steps was measured on both left and right side manually. An additional step is recognized when a footprint of forepaw has no matching footprint of hindpaw or vice versa. A walking task is considered to have additional steps if at least one additional step (on either left or right side) is recognized during the distance used for calculating stride length. The frequency of walking tasks with additional steps for an individual mouse is calculated as (the number of walking tasks with additional steps / total number of walking tasks examined) x 100%.

Statistical analysis

For *Pdss2* conditional knockout mice driven by *Pax2-cre*, embryos with the same genotype at a given stage were pooled. In BrdU assay, the overall cell density (total cell count / area in μm^2) and BrdU index (the number of BrdU positive cells / total cell number) were calculated. In TUNEL assay, the percentage of apoptotic cells is

calculated (the number of apoptotic cells / total cell count). For every embryo, two adjacent coronal sections through cerebellum were examined by counting all recognizable cells in the cerebellum, and the average was taken. Specifically, the average total cell count was 5,000 for control and 4,000 for mutant at E12.5, and 10,000 for control and 5,500 for mutant at E14.5. Cell counting and area measurement were performed using Image J (Ver. 1.43, NIH). Data from 3-4 control or mutant embryos at each stage were used for statistics. Cerebellum coronal sections at E18.5 were also studied by electron microscopy: 4 randomly selected areas (at least 30 cells per area) on each section were examined. Cells with both abnormal mitochondria and strong lysosomal activity (reflected by residual bodies and autophagic-like vacuoles) were considered showing autophagic-like features. The percentage of those autophagic-like (potential or putative autophagic) cells in total cell count of each randomly picked area was calculated. For statistical analysis, independent t-test was performed with SPSS (Ver. 17.0).

For foot print assay of *Pdss2* conditional knockout mice driven by *Pcp2-cre*, the mean stride length was calculated for the left and right side separately. Full factorial ANOVA was performed considering the main effect of side, litter, and genotype. The percentage of walking with additional steps was subjected to ANOVA considering the main effect of litter and genotype.

(Table 1)

Results

Generation of Pdss2 conditional knockout mouse

Detailed procedures of targeting vector construction, ES cell selection, and founder mouse (*Pdss2*$^{f\text{-}E\text{-}Neo/+}$) verification are described in *Supplementary data* (Fig. S1-S2). Those confirmed founders were used in subsequent breeding to generate homozygous floxed mice (*Pdss2*$^{f/f}$) and heterozygous knockout mice with *Pax2-cre* transgenic background (*Pdss2*$^{+/-}$*; Pax2-cre*). By crossing these two mice (*Pdss2*$^{+/-}$*; Pax2-cre* X *Pdss2*$^{f/f}$), tissue specific knockout mice (*Pdss2*$^{f/-}$*; Pax2-cre*) were obtained at a theoretical ratio of 1/4. Another tissue specific knockout mouse line (*Pdss2*$^{f/-}$*; Pcp2-cre*) was generated in a similar way by replacing *Pax2-cre* mouse with *Pcp2-cre* mouse. This breeding strategy is described in *Materials and methods* and illustrated in Fig. S3. The structures of different *Pdss2* alleles and typical genotyping results are demonstrated in Fig. 1A.

The homozygous total knockout mouse (*Pdss2*$^{-/-}$) is embryonic lethal. The oldest *Pdss2*$^{-/-}$ embryo identified is at E9.5, and its morphology resembles normal E6.5 mouse embryo (*data not shown*), so the development of mutant embryo may be blocked at late gastrula stage due to *Pdss2* knockout. The deletion of *Pdss2* exon 2 in heterozygous knockout mice (*Pdss2*$^{+/-}$) was further confirmed by RT-PCR and sequencing (Fig. 1B, Fig. S4). At birth, the PDSS2 protein level in various tissues of *Pdss2*$^{f/-}$*; Pax2-cre* mice was compared with that of litter mate controls (*Pdss2*$^{f/-}$ and *Pdss2*$^{f/+}$) by Western blot (Fig. 1C). Since *Pdss2* knockout is driven by Cre

recombinase in the conditional knockout mouse (*Pdss2$^{f/-}$; Pax2-cre*), it demonstrates a spatial and temporal pattern similar to that of endogenous *Pax2* expression. It has been shown that *Pax2-cre* is mainly expressed in the midbrain-hindbrain region during embryonic development and also in kidney at birth (Ohyama and Groves, 2004). In consistent with this pattern, PDSS2 protein is reduced in kidney of *Pdss2$^{f/-}$; Pax2-cre* mice. Midbrain and pons also demonstrate some degree of PDSS2 decrease, whereas medulla is less affected. More importantly, PDSS2 is almost depleted in the cerebellum of mutant mice, indicating *Pdss2* knockout in cerebellum is successful. Interestingly, PDSS2 protein also decreases in the forelimb muscle, and this may result from the ectopic *Pax2-cre* expression in limb buds during early development (Fig. 2C).

(Fig. 1)

Neonatal death and skeletal muscle defect of Pdss2$^{f/-}$; Pax2-cre mouse

Although the tissue specific knockout mice (*Pdss2$^{f/-}$; Pax2-cre*) can be born alive, they invariably die within the first 36 hr of life. About 50% of them (21 out of 42 mutant mice examined at birth) are identified with cleft palate, which is a common cause of neonatal death in transgenic mice. Cleft palate causes the incomplete separation of oral and nasal cavity, leading to dysphagia and respiratory distress. As demonstrated in Fig. 2A, the most anterior pre-maxilla of the mutant mouse still develops normally, but the two palatine shelves of definitive palate retain a vertical position and fail to fuse along the midline. Therefore, the development of palate may

be blocked around E12.5-13.5 in those mutant mice. On the other hand, even though the mutant mice with normal palate survive longer, they eventually die of starvation, since no milk was found in the stomach. Notably, all mutant mice including those with cleft palate exhibit micrognathia to some extent. Micrognathia is characterized by the under-development of mandible, which is often associated with cleft palate causing respiratory distress and dysphagia in infants. As shown in Fig. 2B, mandible is normally aligned with maxilla in control mice, whereas it becomes much shorter than maxilla in mutant mice. Such mis-alignment of mandible with maxilla impairs feeding, and the posterior displacement of mandible may also result in glossoptosis, leading to pharynx compression and upper airway obstruction. Thus, micrognathia is generally related to the neonatal death of all mutant mice, and cleft palate may further accelerate the death of some mutants.

Since both maxilla and mandible are derived from the first branchial arch (BA1) during development, *Pax2-cre* expression in this region was studied by X-gal staining (Fig. 2C). At E10.5, in addition to midbrain and hindbrain, β-galactosidase activity is also detectable in BA1, and this ectopic Cre expression may result from some neural crest cells migrating from the corresponding hindbrain region where *Pax2-cre* has been expressed. Thus, *Pdss2* knockout may also take place in the cells of BA1, affecting the development of maxilla and mandible in mutant mice. Besides, limb buds also demonstrate *Pax2-cre* expression at E10.5 for unknown reason, and PDSS2 protein is also reduced in forelimb muscle of mutant mice at birth (Fig. 1D). In consistent with reduced PDSS2 protein level, lipid accumulation is evident in the

forelimb skeletal muscle of mutant mice at P0 (Fig. 2D). Such abnormal lipid accumulation in skeletal muscles is also a common symptom of ubiquinone deficiency in human.

(Fig. 2)

Cerebellum hypoplasia and disorganized cell arrangement around birth

Cerebellum hypoplasia is a common feature of all tissue specific knockout mice (*Pdss2$^{f/-}$; Pax2-cre*) around the time of birth. As demonstrated by whole brain X-gal staining at E17.5 (Fig. 3E-G), the size of both midbrain and cerebellum is severely reduced in mutant mice. Specifically, hypoplasia is more severe at the vermis (midline region) than in cerebellar hemispheres. Furthermore, coronal sections of X-gal stained brain also reveal that most cells in the cerebellum are affected by *Pax2-cre* at E17.5 (Fig. 3H-I'), which is consistent with the loss of PDSS2 protein in mutant cerebellum at P0 (Fig. 1D). Thus, the cerebellum hypoplasia observed in *Pdss2$^{f/-}$; Pax2-cre* mouse around birth recapitulates cerebellar atrophy present in some infants with severe ubiquinone deficiency.

At P0, the mutant cerebellum fails to develop normal surface foliations (Fig. 3A1, 3B1), and it contains fewer cells compared with the control cerebellum, especially in the vermis region (Fig. 3A2, 3B2). In addition, the cell stratification is also disorganized. In the normal cerebellum, Purkinje cells have already formed a layer beneath the outmost external granule cell layer (Fig. 3A1), and they can be identified

as parallel clusters by the expression of Purkinje cell marker, CALB-28K (Fig. 3C, 3C'). However, this layer is absent in the mutant cerebellum (Fig. 3B1), and the expression of CALB-28K is not clearly evident (Fig. 3D). This may imply a failure in Purkinje cell maturation or loss of neural progenitors during cerebellum development. Moreover, in contrast to the control cerebellum, in which neurons are evenly distributed and form well defined clusters, most cells in the mutant cerebellum are highly compacted close to the ventricular surface, leaving the dorsal region devoid of cells (Fig. 3A1, 3B1). This disorganization of cell arrangement may represent a defect in the upward migration of neural progenitors from ventricular zone at earlier stages. Therefore, in addition to the overall decrease in cerebellum size, the normal cellular organization is also disrupted in the mutant cerebellum.

(Fig. 3)

The initiation of cerebellum growth retardation during E12.5-14.5 due to defects in radial cell migration

Until E12.5, there is no apparent morphological difference between the control and mutant cerebellum, neither ectopic apoptosis nor reduced cell proliferation is detected (*data not shown*). However, the growth of mutant cerebellum becomes severely retarded since E12.5. During E12.5-14.5, the control cerebellum has dramatic changes in size and shape (Fig. 4A, C). In contrast, the mutant cerebellum fails to expand during this period and retains a similar shape as before, so it appears to be much smaller than the control cerebellum at E14.5 (Fig. 4B, D).

In order to account for this growth retardation, cell proliferation was first compared between control and mutant cerebellum at E12.5 and E14.5 using BrdU assay (Fig. 4E-H). As expected, the proliferating (BrdU positive) cells are concentrated at the sub-ventricular zone in both control and mutant cerebellum, and the percentage of proliferating cells decreases during E12.5-14.5 (Fig. 4N). Based on BrdU index calculation, there is no significant difference in cell proliferation between control and mutant at both stages (Fig. 4N). However, further analysis of cerebellum cell density change during E12.5-14.5 reveals that the cerebellum growth is not only the result of cell proliferation but also depends on the expansion of cerebellum volume. As shown in Fig. 4M, the overall cell density of control cerebellum has decreased by about 50% from E12.5 to E14.5. On the contrary, although the mutant cerebellum has a similar cell density as control at E12.5, it shows a significantly higher overall cell density compared to control at E14.5, indicating a failure in cerebellum expansion during this period. This difference of overall cell density is also evident in the coronal section of control and mutant cerebellum at E14.5 (Fig. 4C-D).

In normal cerebellum, as neuron progenitors migrate upwards from the ventricular zone to the marginal zone, the above intermediate zone containing more differentiated cells is increasing in thickness during E12.5-14.5. Radial cell migration and intermediate zone expansion contribute to the rapid growth of cerebellum, and the overall cell density also decreases during this process because the emerging intermediate zone has a much lower cell density. Therefore, the growth retardation of mutant cerebellum may result from defects in radial cell migration. In fact, the cell

arrangement has already become different between control and mutant since E12.5. In control cerebellum, cells above the proliferating sub-ventricular zone are arranged into parallel columns and demonstrate an obvious trend of radial migration (Fig. 4E). On the contrary, there are fewer cells above the proliferating cell layer, and their arrangement is completely disordered in mutant cerebellum (Fig. 4F). Therefore, at E12.5, neuron progenitors in control cerebellum may leave the proliferating status and start radial migration, whereas this process does not commence in the mutant. Radial glial cells play an important role in neuron progenitor migration because they function as scaffolds for the migrating cells. Therefore, the presence of radial cells was examined by staining for their cell marker, nestin. At E12.5, radial glial cells grow from the ventricular zone and project their process towards the marginal zone, representing the route of radial cell migration in control cerebellum (Fig. 4I, 4I'). Instead, there is only limited amount of radial glial cells in mutant cerebellum at E12.5, and the processes of these cells are much shorter (Fig. 4J, 4J'). Therefore, defects in radial cell growth compromise the radial cell migration, and this may contribute to the growth retardation of mutant cerebellum. Furthermore, as neuron progenitors migrate into the intermediate zone, they start to maturate and express neuron specific markers, such as Tuj1. In the mutant cerebellum, since most neuron progenitors are retained in the sub-ventricular zone, their maturation is also delayed. From Fig. 4K-L, there are more Tuj1 negative cells confined to the sub-ventricular zone even at E14.5, indicating a delay in the expansion of intermediate zone in mutant cerebellum.

(Fig. 4)

Increased ectopic apoptosis companies the progression of cerebellum hypoplasia since E14.5

Although the growth of mutant cerebellum has already become retarded during E12.5-14.5, ectopic apoptosis has not become significant until E14.5, as demonstrated by the percentage of apoptotic cells (Fig. 5A-C). Such ectopic apoptosis becomes more obvious at E15.5 and increases continuously until E18.5. Most apoptotic cells appear as clusters in the intermediate zone of mutant cerebellum (Fig. 5E', G'). Furthermore, with the aid of *ROSA26*^{lacZ} reporter, immunostaining of β-galactosidase demonstrates that apoptosis is co-localized with the region where Cre has been expressed in mutant cerebellum (Fig. 5K'). In addition to ectopic apoptosis, neuroblast proliferation is also reduced in mutant cerebellum, and these neuroblasts are also affected by *Pax2-cre*, as revealed by X-gal staining (Fig. 5H-I').

Therefore, the increased ectopic apoptosis since E14.5 further aggravates the growth retardation initiated at earlier developmental stages (E12.5-14.5) and eventually leads to severe cerebellum hypoplasia in the mutant mouse. At birth, the mutant cerebellum contains fewer cells due to neuron loss by intensive apoptosis during E14.5-P0. In addition, the normal cellular organization is not established, as most cells are compacted close to the ventricular zone. Such morphological defects may reflect the impairment of radial cell migration during E12.5-14.5. Moreover, as the major cause of neuron loss, apoptosis is co-localized with *Pax2-cre* expression, so

Pdss2 knockout is likely to cause neuron loss in the mutant cerebellum.

(Fig. 5)

Normal Fgf8 expression in the isthmus of mutant embryo before E11.5

Fibroblast growth factor 8 (FGF8) released by isthmus during E9.5-12.5 promotes cell survival and differentiation in cerebellum. Considering that the development of radial glial cell is affected in *Pdss2$^{f/-}$; Pax2-cre* embryos at E12.5, and *Pax2* plays an important role in *Fgf8* expression, *Pdss2* knockout may impair cerebellum development indirectly via reduced FGF8 production. Nevertheless, *in situ* hybridization shows that normal *Fgf8* expression at isthmus is maintained in the mutant embryo until E11.5 (Fig. 6). Thus, the development defect observed at E12.5 and afterwards is not caused by reduced FGF8 level at earlier stages.

(Fig. 6)

Abnormal mitochondria and autophagic-like structures in the cells of mutant cerebellum

The sub-cellular morphology of mutant cerebellum was studied by transmission electron microscope (TEM) at E18.5. In consistent with TUNEL assay, massive apoptotic cells are also evident in the mutant cerebellum (Fig. 7C). The mitochondria in control cerebellum cells possess smooth membrane with regular cristae, and the matrix is homogeneous and electron-dense (Fig. 7B). In contrast, abnormal

mitochondria are found to accumulate in those surviving cells of mutant cerebellum: they are swollen and devoid of cristae, and the mitochondrial matrix becomes pale and loses electron density (Fig. 7D). Interestingly, in many of those cells that still survive, defective mitochondria are engulfed by rER (Fig. 7E), and elevated lysosomal activity is also evident by increased residual bodies (Fig. 7F-G). These morphological features imply that autophagy of abnormal mitochondria may be involved, and the percentage of cells with such autophagic-like structures has significantly increased in the mutant cerebellum (Fig. 7H). Consequently, mitochondrial defect may trigger the apoptosis, whereas autophagic-like vacuoles may also arise to remove abnormal mitochondria and promote cell survival in the mutant cerebellum.

(Fig. 7)

Gradual development of ataxia in Pdss2$^{f/-}$; Pcp2-cre mouse

Since the neonatal death of *Pdss2$^{f/-}$; Pax2-cre* mouse precludes further study at adult stage, a more specific deleter mouse strain, *Pcp2-cre*, was used to produce another Pdss2 conditional knockout mouse (*Pdss2$^{f/-}$; Pcp2-cre* or *Pdss2$^{f/-}$; ROSA26$^{lacZ/+}$; Pcp2-cre*). In *Pcp2-cre* mouse, Cre recombinase is expressed only in cerebellar Purkinje cells and retinal bipolar neurons, and the expression starts at day 7 after birth (P7) and reaches its peak level at P15 (Zhang et al., 2004). Thus, this *Pcp2-cre* mouse allows further anaylsis of *Pdss2* function in cerebellum at postnatal stages. The mutant mice (*Pdss2$^{f/-}$; Pcp2-cre*) remain healthy and do not show any

abnormal behavior at 4.5 months (Video 1-2). Nevertheless, failure in motor coordination during walking and incapability of maintaining balance on a rod have been observed at 9.5 months (Video 3-4). This phenotype resembles ataxia in human ubiquinone deficiency, and it becomes more severe in elder mutant mice. At 1 year old, the ambulation of mutant mice was assessed by footprinting assay, and the results were compared with their control litter mates (Fig. 8). The steps of control mice are evenly spaced, and the forepaw tends to overlap well with the hindpaw on the same side (Fig. 8A). In contrast, the stride length of mutant mice is shorter and more variable, and additional steps made by both forepaw and hindpaw are more frequent than control over the same walking distance (Fig. 8B). Even though the mutant mice take more steps in order to compensate motor incoordination, they sometimes still fail to maintain balance and slip to one side (Fig. 8C). Similarly, statistical analysis reveals that increased frequency of additional steps during walking and shortened average stride length (Fig. 8D, E). Furthermore, the defect is not uni-lateral, as the mean stride length of left and right side is not significantly different ($p = 0.786$ by ANOVA) for both control and mutant mice. In summary, *Pdss2*$^{f/-}$*; Pcp2-cre* mice develop a progressive ataxia phenotype comparable to human ubiquinone deficiency, as they become aged.

(Video. 1-4)

(Fig. 8)

Progressive loss of cerebellum Purkinje cells and neuronal death by apoptosis may

lead to the ataxia in aged Pdss2$^{f/-}$; Pcp2-cre mouse

In mutant mice, *Pcp2-cre* drives *Pdss2* knockout in Purkinje cells, whose defects are associated with cerebellar ataxia, so Purkinje cells are examined at different stages. At 1 month old, there is no obvious difference in the pattern or amount of Purkinje cells between control (*Pdss2$^{f/+}$; ROSA26$^{lacZ/+}$; Pcp2-cre*) and mutant (*Pdss2$^{f/-}$; ROSA26$^{lacZ/+}$; Pcp2-cre*) cerebellum, as shown by both X-gal staining and immunostaining for Purkinje cells (Fig. 9A-F). However, at 6 months old, the number of Purkinje cells has significantly decreased in the mutant cerebellum compared to that of control, as demonstrated by reduced blue signal of X-gal staining and very few cells positive for Purkinje cell marker (Fig. 9G-L). In consistent with the onset time of ataxia, increased apoptosis also starts at 6 months in the mutant cerebellum (Fig. 10A-D), and more dispersed apoptosis can be detected at 9.5 months (Fig. 10E-H) by TUNEL assay. Similarly, electron microscopy also reveals apoptotic cells and swollen mitochondria in mutant mouse cerebellum at 8 months (Fig. 10I-L). Therefore, the gradual loss of Purkinje cells and initiation of diffusive neuron death by apoptosis may both contribute to atxia in aged *Pdss2$^{f/-}$; Pcp2-cre* mice.

(Fig. 9)

(Fig. 10)

Discussion

The *Pdss2*$^{f/-}$*; Pax2-cre* mouse generated in this study not only reveals the important function of ubiquinone during mouse embryonic development but also recaptures some important features of human ubiquinone deficiency. Ubiquinone is known to play an essential role in mouse embryo development because complete knockout of *Coq7*, a gene involved in ubiquinone synthesis, results in embryo degeneration at E12.5 (Levavasseur et al., 2001). Similarly, the total knockout mouse (*Pdss2*$^{-/-}$) we generated is also embryonic lethal around E9.5, and cerebellum hypoplasia is observed in all *Pdss2*$^{f/-}$*; Pax2-cre* mice at birth, indicating a growth defect during embryonic development. In human, cerebellar atrophy is a common symptom of many subtypes of ubiquinone deficiency, and it may even appear at infantile stage (Lopez et al., 2006). Severe cerebellum hypoplasia in neonatal *Pdss2*$^{f/-}$*; Pax2-cre* mice just recapitulates the similar feature in the human disease. Furthermore, abnormal lipid accumulation in skeletal muscle is another common symptom caused by ubiquinone deficiency, which may result from a defect in fatty acid metabolism. Because mitochondrial respiration is blocked due to ubiquinone deficiency, NADH generated by tricarboxylic acid (TCA) cycle cannot be converted to NAD^+, which is an indispensible electron acceptor in lipid β-oxidation (Boitier et al., 1998; Ogasahara et al., 1989). In our case, excessive lipid accumulation is also found in limb muscles of newborn mutant mice.

Recently, a similar *Pdss2* conditional knockout mouse (*Pdss2*$^{loxp/loxp}$) has been

developed (Peng et al., 2008), in which *Pdss2* exon 2 is also flanked by two LoxP sites. Before this mouse was reported, we had independently generated the *Pdss2* floxed mouse (*Pdss2*$^{f/f}$) using a different targeting vector (see *Supplementary data*). When the *Pdss2*$^{loxp/loxp}$ mouse is crossed to a podocyte specific deleter mouse (*Podocin-cre*), the resulting tissue specific knockout mouse develops a kidney disease comparable to that of *kd/kd* mouse, demonstrating that exon 2 is essential for PDSS2 function. Furthermore, ubiquinone decrease is evident in specific tissues of the conditional knockout mouse (Peng et al., 2008), and *kd/kd* mouse has demonstrated improvement following oral CoQ_{10} treatment (Saiki et al., 2008). Thus, similar to the situation in human, the causative relation between defective PDSS2 protein and ubiquinone deficiency has been strongly implied in mouse. In our case, PDSS2 protein is deficient in limb muscle and almost depleted in cerebellum of the *Pdss2*$^{f/-}$*; Pax2-cre* mice, as shown by Western blot. Therefore, it is very likely that cerebellum hypoplasia observed in our mutant mice also results from PDSS2 based ubiquinone deficiency, although we cannot exclude the possibility that PDSS2 may have other unknown funtions during cerebellum development in addition to ubiquinone synthesis.

The pathogenesis of cerebellum hypoplasia has been studied during embryonic development for *Pdss2*$^{f/-}$*; Pax2-cre* mice. Because the temporal and spatial control of *Pdss2* knockout is achieved by *Pax2-cre*, a reporter (*ROSA26*^{lacZ}) is introduced so that the regions of *Pdss2* deletion can be revealed by β-galactosidase expression. *Pax2* is initially expressed across isthmus at E8.0 in normal mouse embryo (Echevarria et al.,

2005), and β-galactosidase activity has become evident in the hindbrain region since E9.5 in *Pax2-cre* mouse (Ohyama and Groves, 2004). In *Pdss2*$^{f/-}$*; Pax2-cre* mice, due to combined effect of cell proliferation and migration during cerebellum development, the actual region affected by *Pdss2* knockout is further expanded to include most cells within cerebellum around the time of birth, which can be demonstrated by X-gal staining at E17.5. However, there is no apparent morphological difference between the cerebellar plate of control and mutant embryos before E11.5, and this can be accounted by a time lapse from the initiation of *Pax2-cre* expression to the onset of cellular defect due to *Pdss2* knockout. E12.5-14.5 is a critical period of cerebellum development, and it is also the time when cerebellum growth retardation starts to appear in mutant embryos. One immediate cause of such defect is the failure in neuroblast radial migration and intermediate zone expansion, and delay or impairment of radial glial cell development seems to be a possible underlying reason. Interestingly, neither reduced cell proliferation nor ectopic apoptosis makes significant contribution to cerebellum growth retardation during this period, but they become the key factors leading to cerebellum hypoplasia after E14.5. Perhaps, ectopic apoptosis in the cells of intermediate zone is the most important factor, because impaired cell proliferation in the same region may also result from the loss of proliferating cells by apoptosis. As a result of extensive apoptosis of neurons in the intermediate zone, there are few cells left between the marginal zone and ventricular zone in mutant cerebellum at P0, and the normal cellular organization is also lost. In consistent with our results, apoptosis has been observed in skeletal muscles (Di Giovanni et al., 2001) and cultured skin

fibroblasts (Rodriguez-Hernandez et al., 2009) from ubiquinone deficient patients.

Because of the important function of FGF8 in cerebellum and its close relation to *Pax2* gene during early embryonic development, the effect of *Pdss2* knockout on FGF8 production is also investigated for *Pdss2*$^{f/-}$*; Pax2-cre* mice. Isthmus is an important secondary organizer at the junction between midbrain and hindbrain during early development. It emanates WNT1 to the anterior part (midbrain) and FGF8 to the posterior part (developing cerebellum and rhombomeres) from E9.5 to E12.5 (Joyner et al., 2000). FGF8 is a long-range diffusible growth factor that promotes cell proliferation and differentiation in the prospective cerebellum (Partanen, 2007). Thus, in *Fgf8*$^{f/-}$*; En1-cre* conditional knockout mouse, the entire cerebellum is absent at E17.5 due to ectopic apoptosis since E9.0 (Chi et al., 2003). The establishment of isthmus organizer requires the participation of *Otx2*, *Gbx2*, *Pax2*, *En1*, and other genes expressed at the midbrain-hindbrain boundary. *Pax2* is a prerequisite for the initial expression of *Fgf8* at isthmus, whereas the proper gradient of OTX2 and GBX2 maintains its stable expression (Ye et al., 2001). Therefore, defects of *Pax2* also result in abnormal cerebellum development, as demonstrated by *Pax2*^{1Neu} mutant mouse, which shows cerebellum deletion at E14.5 owing to the loss of isthmus region at E12.5 (Favor et al., 1996). In the present study, *Pdss2*$^{f/-}$*; Pax2-cre* mice also represent cerebellum hypoplasia due to ecotpic apoptosis, but the defect is less severe than those described above. As Cre recominase is induced by *Pax2* expression, *Pdss2* knockout in the *Pax2* positive cells at isthmus may influence later cerebellum development via reduced FGF8 production, even though there is no appearant

abnormality before E11.5. However, *in situ* hybridization illustrates that *Fgf8* expression at isthmus is normal in the mutant mouse until E11.5. Therefore, the contribution of reduced FGF8 to cerebellum hypoplasia can be excluded. Perhaps, *Pdss2* knockout has not caused substantial cellular defect to alter isthmic FGF8 production before E12.5.

The *Pdss2*$^{f/-}$*; Pax2-cre* mouse suffers from neonatal death, precluding further study at postnatal stages. Although cleft palate and micrognathia are considered as the main reasons, other factors may also contribute to the neonatal death. For example, renal failure may cause death in infants with ubiquinone deficiency (Lopez et al., 2006), and *Pax2-cre* is also strongly expressed in kidney (Ohyama and Groves, 2004). Even though edema has not been observed in newborn mutant mice, the contribution of kidney disorder cannot be excluded. Besides, tongue plays an important role in the voluntary part of swallowing (McConnel et al., 1988), and its anterior portion also arises from the first branchial arch (the same origin as mandible), so defects in tongue muscle or innervation may cause dysphagia in the mutant mouse. Nevertheless, micrognathia and cleft palate are closely associated and often manifest simultaneously in Treacher Collins syndrome, Nager syndrome, or Pierre Robin sequence, and infants affected by those diseases also demonstrate dysphagia and respiratory distress (Posnick and Ruiz, 2000). Furthermore, microganthia and cleft palate can be caused by various genetic disorders, but they usually result from developmental defects in the first or second branchial arch (Marszalek et al., 2002). However, symptoms such as microganthia and cleft palate have not been reported in ubiquinone deficient patients.

It has been demonstrated that the *Pax2-cre* mouse used in this study has an ectopic Cre expression in the first branchial arch at E9.5 (Ohyama and Groves, 2004), and β-galactosidase activity is also detectable in the same region at E10.5 by X-gal staining based on our results. Perhaps, unexpected *Pdss2* knockout in the first branchial arch may result from this ectopic *Pax2-cre* expression. In addition, during E9.5-11.5, the migrating neural crest cells from hindbrain where *Pax2-cre* is expressed may also contribute to *Pdss2* knockout in the first branchial arch. As a result, the development of mandible and maxilla is affected, leading to micrognathia and cleft palate in the mutant mouse.

In order to circumvent the problems caused by neonatal death in *Pdss2*$^{f/-}$*; Pax2-cre* mice, we restricted the region and delayed the onset time of *Pdss2* knockout by using a *Pcp2-cre* deleter mouse. In this new *Pdss2* conditional knockout mouse (*Pdss2*$^{f/-}$*; Pcp2-cre*), *cre* expression is confined to cerebellar Purkinje cells and only starts from P7 (Zhang et al., 2004), so characterization on adult mutant mice becomes possible. We chose this *Pcp2-cre* mouse also because Purkinje cells are the major inhibitory neurons in cerebellum and play an important role in motor coordination (Mauk, 1997). Consequently, lesions of Purkinje cells may cause cerebellar ataxia, which is also a hallmark of human ubiquinone deficiency in many adult patients (Lamperti et al., 2003). With the *ROSA26*^{lacZ} reporter, X-gal staining demonstrates that β-galactosidase has been expressed in most cerebellum Purkinje cells by 1 month (Fig. 9A, D), indicating *Pdss2* knockout has already started at that time. Nevertheless, just as the situation in the cerebellum of *Pdss2*$^{f/-}$*; Pax2-cre* mice before E12.5, the

effect of *Pdss2* knockout may be delayed since the Purkinje cells are still morphologically normal in 1 month old *Pdss2$^{f/-}$; Pcp2-cre* mice. Similarly, the sign of cerebellar ataxia has not been observed even at 4.5 months. However, Purkinje cells are mostly depleted in the cerebellum of *Pdss2$^{f/-}$; Pcp2-cre* mouse at 6 months (Fig. 9G-L), and features of cerebellar ataxia also develops about 3 months later (Video 3-4). By quantitative analysis of foot printing for aged mutant mice, impaired motor coordination is indicated by increased frequency of additional steps during walking, whereas shortened stride length reveals compromised ambulation capability. Therefore, unlike the *Pdss2$^{f/-}$; Pax2-cre* mouse which demonstrates a developmental defect in cerebellum, the *Pdss2$^{f/-}$; Pcp2-cre* mouse represents an example of neuron degeneration. More importantly, it recapitulates the progressive nature of ubiquinone deficiency and may serve as a better model for the ataxia form of human ubiquinone deficiency in adults. During the pathogenic course, Purkinje cell degeneration and subsequent diffusive neuron death by apoptosis may both contribute to the development of ataxia. Although Purkinje cells have been almost depleted in mutant cerebellum at 6 months, there has not been any significant ectopic apoptosis detected before that time. Furthermore, the pattern of apoptosis at later stages (6 months to 9.5 months) does not entirely correlate to the normal anatomical location of Purkinje cells (Fig. 10D, H). As a result, Purkinje cell degeneration may not be attributed to ectopic apoptosis, and the late onset of diffusive apoptosis may reflect other neuron death secondary to Purkinje cell loss. The mechanism of Purkinje cell degeneration and rescue experiments using ubiquinone therapy in *Pdss2$^{f/-}$; Pcp2-cre* mice will be of

great interest in future study.

Conclusions

In conclusion, this study exploits the use of conditional knockout mouse to investigate the cerebellum defect of human ubiquinone deficiency. One tissue specific knockout mouse (*Pdss2*$^{f/-}$*; Pax2-cre*) demonstrates cerebellum hypoplasia at birth, which resembles the cerebellum atrophy commonly observed in ubiquinone deficient infants. Moreover, by studying the pathogenesis of cerebellum hypoplasia during embryonic development, it reveals that *Pdss2* knockout results in early cell migration defect, impaired cell proliferation, and increased ectopic apoptosis. Consistent with previous studies, mitochondrial defect may be the cause of apoptosis, and autophagic-like vacuolization may imply the involvement of mitophagy. The other tissue specific knockout mouse (*Pdss2*$^{f/-}$*; Pcp2-cre*) demonstrates gradual loss of cerebellum Purkinje cells and develops cerebellar ataxia at old age, which recapitulates a more common ataxia form of ubiquinone deficiency in adults. To our knowledge, this is the first study that focuses on the cerebellum symptoms of ubiquinone deficiency using conditional knockout mouse models, and it also directly reflects the function of *Pdss2* in cerebellar development. This study brings some insights into the pathogenesis of the cerebellar defect caused by ubiquinone deficiency.

Acknowledgments

We thank Ms. Sheila Tsang for her great help in blastocyst injection. We also thank Dr. A Groves for providing *Pax2-Cre* mice and Prof. K. SE. Cheah in the Department of Biochemistry, University of Hong Kong, for giving us *Pax2-cre* deleter mouse line and *Fgf8* probe plasmid. This work was supported by grants from the Hong Kong Research Grants Council (HKU 7321/04M; HKU 7636/05M) to J.D.H., and partial by a RGC Group Research Project (HKUST6/CRF/08).

Disclosure Statement

We declare that there is no actual or potential conflict of interest among all authors.

Reference

Barisoni, L., Madaio, M.P., Eraso, M., Gasser, D.L., Nelson, P.J., 2005. The kd/kd mouse is a model of collapsing glomerulopathy. J Am Soc Nephrol. 16**,** 2847-51.

Boitier, E., Degoul, F., Desguerre, I., Charpentier, C., Francois, D., Ponsot, G., Diry, M., Rustin, P., Marsac, C., 1998. A case of mitochondrial encephalomyopathy associated with a muscle coenzyme Q10 deficiency. J Neurol Sci. 156**,** 41-6.

Carson, F.L., 1990. Histotechnology : a self instructional text. Vol., ASCP Press, Chicago.

Chi, C.L., Martinez, S., Wurst, W., Martin, G.R., 2003. The isthmic organizer signal FGF8 is required for cell survival in the prospective midbrain and cerebellum. Development. 130**,** 2633-44.

Crossley, P.H., Martin, G.R., 1995. The mouse Fgf8 gene encodes a family of polypeptides and is expressed in regions that direct outgrowth and patterning in the developing embryo. Development. 121**,** 439-51.

Di Giovanni, S., Mirabella, M., Spinazzola, A., Crociani, P., Silvestri, G., Broccolini, A., Tonali, P., Di Mauro, S., Servidei, S., 2001. Coenzyme Q10 reverses pathological phenotype and reduces apoptosis in familial CoQ10 deficiency. Neurology. 57**,** 515-8.

Echevarria, D., Belo, J.A., Martinez, S., 2005. Modulation of Fgf8 activity during vertebrate brain development. Brain Res Brain Res Rev. 49**,** 150-7.

Farley, F.W., Soriano, P., Steffen, L.S., Dymecki, S.M., 2000. Widespread

recombinase expression using FLPeR (flipper) mice. Genesis. 28**,** 106-10.

Favor, J., Sandulache, R., Neuhauser-Klaus, A., Pretsch, W., Chatterjee, B., Senft, E., Wurst, W., Blanquet, V., Grimes, P., Sporle, R., Schughart, K., 1996. The mouse Pax2(1Neu) mutation is identical to a human PAX2 mutation in a family with renal-coloboma syndrome and results in developmental defects of the brain, ear, eye, and kidney. Proc Natl Acad Sci U S A. 93**,** 13870-5.

Fung, J.M., Smith, R., Brown, M.A., Lau, S.H., Xie, D., Lau, G.K., Guan, X.Y., 2009. Identification and characterization of a novel melanoma tumor suppressor gene on human chromosome 6q21. Clin Cancer Res. 15**,** 797-803.

Gerfen, C.R., Rogawski, M.A., Sibley, D.R., 2007. Short protocols in neuroscience : systems and behavioral methods : a compendium of methods from Current protocols in neuroscience. Vol., John Wiley.

Joyner, A.L., Liu, A., Millet, S., 2000. Otx2, Gbx2 and Fgf8 interact to position and maintain a mid-hindbrain organizer. Curr Opin Cell Biol. 12**,** 736-41.

Kimmel, C.A., Trammell, C., 1981. A rapid procedure for routine double staining of cartilage and bone in fetal and adult animals. Stain Technol. 56**,** 271-3.

Klingenberg, M., Echtay, K.S., 2001. Uncoupling proteins: the issues from a biochemist point of view. Biochim Biophys Acta. 1504**,** 128-43.

Lalani, S.R., Vladutiu, G.D., Plunkett, K., Lotze, T.E., Adesina, A.M., Scaglia, F., 2005. Isolated mitochondrial myopathy associated with muscle coenzyme Q10 deficiency. Arch Neurol. 62**,** 317-20.

Lamperti, C., Naini, A., Hirano, M., De Vivo, D.C., Bertini, E., Servidei, S., Valeriani,

M., Lynch, D., Banwell, B., Berg, M., Dubrovsky, T., Chiriboga, C., Angelini, C., Pegoraro, E., DiMauro, S., 2003. Cerebellar ataxia and coenzyme Q10 deficiency. Neurology. 60**,** 1206-8.

Levavasseur, F., Miyadera, H., Sirois, J., Tremblay, M.L., Kita, K., Shoubridge, E., Hekimi, S., 2001. Ubiquinone is necessary for mouse embryonic development but is not essential for mitochondrial respiration. J Biol Chem. 276**,** 46160-4.

Lewandoski, M., Meyers, E.N., Martin, G.R., 1997. Analysis of Fgf8 gene function in vertebrate development. Cold Spring Harb Symp Quant Biol. 62**,** 159-68.

Lopez, L.C., Schuelke, M., Quinzii, C.M., Kanki, T., Rodenburg, R.J., Naini, A., Dimauro, S., Hirano, M., 2006. Leigh syndrome with nephropathy and CoQ10 deficiency due to decaprenyl diphosphate synthase subunit 2 (PDSS2) mutations. Am J Hum Genet. 79**,** 1125-9.

Marszalek, B., Wojcicki, P., Kobus, K., Trzeciak, W.H., 2002. Clinical features, treatment and genetic background of Treacher Collins syndrome. J Appl Genet. 43**,** 223-33.

Mauk, M.D., 1997. Roles of cerebellar cortex and nuclei in motor learning: contradictions or clues? Neuron. 18**,** 343-6.

McConnel, F.M., Cerenko, D., Mendelsohn, M.S., 1988. Manofluorographic analysis of swallowing. Otolaryngol Clin North Am. 21**,** 625-35.

McLeod, M.J., 1980. Differential staining of cartilage and bone in whole mouse fetuses by alcian blue and alizarin red S. Teratology. 22**,** 299-301.

Meganathan, R., 2001. Ubiquinone biosynthesis in microorganisms. FEMS Microbiol

Lett. 203**,** 131-9.

Mollet, J., Giurgea, I., Schlemmer, D., Dallner, G., Chretien, D., Delahodde, A., Bacq, D., de Lonlay, P., Munnich, A., Rotig, A., 2007. Prenyldiphosphate synthase, subunit 1 (PDSS1) and OH-benzoate polyprenyltransferase (COQ2) mutations in ubiquinone deficiency and oxidative phosphorylation disorders. J Clin Invest. 117**,** 765-72.

Musumeci, O., Naini, A., Slonim, A.E., Skavin, N., Hadjigeorgiou, G.L., Krawiecki, N., Weissman, B.M., Tsao, C.Y., Mendell, J.R., Shanske, S., De Vivo, D.C., Hirano, M., DiMauro, S., 2001. Familial cerebellar ataxia with muscle coenzyme Q10 deficiency. Neurology. 56**,** 849-55.

Ogasahara, S., Engel, A.G., Frens, D., Mack, D., 1989. Muscle coenzyme Q deficiency in familial mitochondrial encephalomyopathy. Proc Natl Acad Sci U S A. 86**,** 2379-82.

Ohyama, T., Groves, A.K., 2004. Generation of Pax2-Cre mice by modification of a Pax2 bacterial artificial chromosome. Genesis. 38**,** 195-9.

Partanen, J., 2007. FGF signalling pathways in development of the midbrain and anterior hindbrain. J Neurochem. 101**,** 1185-93.

Peng, M., Jarett, L., Meade, R., Madaio, M.P., Hancock, W.W., George, A.L., Jr., Neilson, E.G., Gasser, D.L., 2004. Mutant prenyltransferase-like mitochondrial protein (PLMP) and mitochondrial abnormalities in kd/kd mice. Kidney Int. 66**,** 20-8.

Peng, M., Falk, M.J., Haase, V.H., King, R., Polyak, E., Selak, M., Yudkoff, M.,

Hancock, W.W., Meade, R., Saiki, R., Lunceford, A.L., Clarke, C.F., Gasser, D.L., 2008. Primary coenzyme Q deficiency in Pdss2 mutant mice causes isolated renal disease. PLoS Genet. 4**,** e1000061.

Posnick, J.C., Ruiz, R.L., 2000. Treacher Collins syndrome: current evaluation, treatment, and future directions. Cleft Palate Craniofac J. 37**,** 434.

Quinzii, C.M., DiMauro, S., Hirano, M., 2007a. Human coenzyme Q10 deficiency. Neurochem Res. 32**,** 723-7.

Quinzii, C.M., Hirano, M., DiMauro, S., 2007b. CoQ10 deficiency diseases in adults. Mitochondrion. 7 Suppl**,** S122-6.

Rodriguez-Hernandez, A., Cordero, M.D., Salviati, L., Artuch, R., Pineda, M., Briones, P., Gomez Izquierdo, L., Cotan, D., Navas, P., Sanchez-Alcazar, J.A., 2009. Coenzyme Q deficiency triggers mitochondria degradation by mitophagy. Autophagy. 5**,** 19-32.

Rotig, A., Appelkvist, E.L., Geromel, V., Chretien, D., Kadhom, N., Edery, P., Lebideau, M., Dallner, G., Munnich, A., Ernster, L., Rustin, P., 2000. Quinone-responsive multiple respiratory-chain dysfunction due to widespread coenzyme Q10 deficiency. Lancet. 356**,** 391-5.

Rotig, A., Mollet, J., Rio, M., Munnich, A., 2007. Infantile and pediatric quinone deficiency diseases. Mitochondrion. 7 Suppl**,** S112-21.

Saiki, R., Nagata, A., Kainou, T., Matsuda, H., Kawamukai, M., 2005. Characterization of solanesyl and decaprenyl diphosphate synthases in mice and humans. FEBS J. 272**,** 5606-22.

Saiki, R., Lunceford, A.L., Shi, Y., Marbois, B., King, R., Pachuski, J., Kawamukai, M., Gasser, D.L., Clarke, C.F., 2008. Coenzyme Q10 supplementation rescues renal disease in Pdss2kd/kd mice with mutations in prenyl diphosphate synthase subunit 2. Am J Physiol Renal Physiol. 295**,** F1535-44.

Salviati, L., Sacconi, S., Murer, L., Zacchello, G., Franceschini, L., Laverda, A.M., Basso, G., Quinzii, C., Angelini, C., Hirano, M., Naini, A.B., Navas, P., DiMauro, S., Montini, G., 2005. Infantile encephalomyopathy and nephropathy with CoQ10 deficiency: a CoQ10-responsive condition. Neurology. 65**,** 606-8.

Soriano, P., 1999. Generalized lacZ expression with the ROSA26 Cre reporter strain. Nat Genet. 21**,** 70-1.

Turunen, M., Olsson, J., Dallner, G., 2004. Metabolism and function of coenzyme Q. Biochim Biophys Acta. 1660**,** 171-99.

Walter, L., Nogueira, V., Leverve, X., Heitz, M.P., Bernardi, P., Fontaine, E., 2000. Three classes of ubiquinone analogs regulate the mitochondrial permeability transition pore through a common site. J Biol Chem. 275**,** 29521-7.

Wilkinson, D.G., 1992. In Situ Hybridisation: A Practical Approach. Vol., IRL Press at Oxford University Press, Oxford.

Wu, S., Ying, G., Wu, Q., Capecchi, M.R., 2008. A protocol for constructing gene targeting vectors: generating knockout mice for the cadherin family and beyond. Nat Protoc. 3**,** 1056-76.

Ye, W., Bouchard, M., Stone, D., Liu, X., Vella, F., Lee, J., Nakamura, H., Ang, S.L.,

Busslinger, M., Rosenthal, A., 2001. Distinct regulators control the expression of the mid-hindbrain organizer signal FGF8. Nat Neurosci. 4**,** 1175-81.

Zhang, X.M., Ng, A.H., Tanner, J.A., Wu, W.T., Copeland, N.G., Jenkins, N.A., Huang, J.D., 2004. Highly restricted expression of Cre recombinase in cerebellar Purkinje cells. Genesis. 40**,** 45-51.

Figure and video legeneds

Fig. 1: Generation of *Pdss2* conditional knockout mouse (*Pdss2$^{f/-}$; Pax2-cre*). **A:** The structures of different *Pdss2* alleles involved in the study are illustrated along with genotyping primers (upper panel). The sequences of those primers are given in *Table 1*. Typical PCR genotyping results are shown in the lower panel: *Pdss2^{f}* (584 bp) and *Pdss2^{+}* (422 bp) alleles were differentiated by CKO-f & CKO-r. *Pdss2^{-}* allele (522 bp) and *Cre* transgene (270 bp) were detected by KO-f & KO-r and Cre-f & Cre-r, respectively. These three sets of primers were used to identify the tissue specific knockout mouse. In this example, the four mice were genotyped as followed: 1 = *Pdss2$^{f/-}$; Pax2-cre*, 2 = *Pdss2$^{f/+}$; Pax2-cre*, 3 = *Pdss2$^{f/+}$*, 4 = *Pdss2$^{f/-}$*. Because genotyping for *Cre* is based on detecting *Cre* transgene without distinguishing *Pax2-cre* and *Pcp2-cre*, the same genotyping method also applies to another conditional knockout mouse (*Pdss2$^{f/-}$; Pcp2-cre*). **B:** The cDNA structures (long isoform) of *Pdss2^{+}* and *Pdss2^{-}* are compared in the upper panel, and a representative RT-PCR result is shown below. By RT-f1 & RT-r5, there was a gap of 135 bp between *Pdss2^{+}* (798 bp) and *Pdss2^{-}* (663 bp) alleles due to the loss of exon 2. Sequencing of the two RT-PCR products by *Pdss2*-Ex3-seq-r further demonstrated that the 135 bp gap represents the deleted exon 2 in *Pdss2^{-}* mRNA (*Supplementary data, Fig. S4*). **C:** Western blot results comparing PDSS2 protein in various tissues among *Pdss2$^{f/+}$* (C), *Pdss2$^{f/-}$* (H), *Pdss2$^{f/-}$; Pax2-cre* (M) mice from the same litter. PDSS2 is detected at about 37 KDa, and α-tubulin at 55 KDa as an internal control.

Fig. 2: Neonatal death and lipid accumulation in skeletal muscle. **A-B:** Whole mount skeleton preparation stained with Alcian blue & Alizarin red S (P0). In panel A, cleft palate is demonstrated by the yellow arrows in the ventral view of palate (mandible removed). Micrognathia is illustrated in panel B. The red arrow indicates that the shorter mandible fails to align with the maxilla in mutant mouse. Panels (A-B) are representative results of 5 control and mutant mice. **C:** Whole mount X-gal staining of *Pax2-cre* embryo at E10.5 (M: midbrain, H: hindbrain, FLB: forelimb bud). **C':** A para-sagittal section through the first branchial arch (squared region in C), counter stained with nuclear fast red. Panels (C, C') are representative images of 4 mice. **D:** Sudan black B staining counter stained by nuclear fast red (P0). The black dots represent lipid droplets in the mutant (*Pdss2$^{f/-}$; Pax2-cre*). Panels in this figure are representatives of at least 3 mice in both control and mutant groups. Scale bars: 1.5 mm in (A); 2 mm in (B); 1 mm in (C); 100 μm in (C') and (D).

Fig. 3: Cerebellum hypoplasia around the time of birth. **A-B:** Coronal section of cerebellum at birth (H&E stain). Control: *Pdss2$^{f/+}$* (A), mutant: *Pdss2$^{f/-}$; Pax2-cre* (B). A1-A2 and B1-B2 are magnifications of the squared areas in A and B, respectively. Panels (A-B) are representatives of 4 control and 4 mutant mice. **C-D:** Immunostaining of Purkinje cells by anti-CALB-28K antibody at P0 (DAB counter stained with hematoxylin). Control: *Pdss2$^{f/+}$* (C), mutant: *Pdss2$^{f/-}$; Pax2-cre* (D). C' is a magnification of the squared area in C, and the yellow arrows point to Purkinje cell clusters. Panels (C-D) are representatives of 3 control and 3 mutant mice. **E-G:** Whole mount X-gal staining of mouse brain at E17.5. Only the midbrain and cerebellum are shown (dorsal view). Positive control: *Pdss2$^{f/+}$; ROSA26$^{lacZ/+}$; Pax2-cre*

(E), mutant: *Pdss2$^{f/-}$; ROSA26$^{lacZ/+}$; Pax2-cre* (F), negative control: *Pdss2$^{f/+}$; Pax2-cre* (G). The yellow arrow indicates severe hypoplasia of vermis in mutant cerebellum (F). **H-I:** Coronal section of stained cerebellum shown in E and F, counter stained by nuclear fast red. **I':** A magnification of the squared area in I. Panels (E-I') are representatives of 3 control and 3 mutant mice. Scale bars: 300 μm in (A-B); 150 μm in (A1-A2), (B1-B2), (C), (H-I); 75 μm in (C'), (D), (I'); 1 mm in (E-G).

Fig. 4: Cerebellum growth retardation from E12.5 to E14.5. **A-B:** Coronal section of cerebellum at E12.5 (H&E stain). Control: *Pdss2$^{f/+}$* (A), mutant: *Pdss2$^{f/-}$; Pax2-cre* (B). **C-D:** Coronal section of cerebellum at E14.5 (H&E stain). Control: *Pdss2$^{f/+}$* (C), mutant: *Pdss2$^{f/-}$; Pax2-cre* (D). **E-F:** BrdU assay of cerebellum at E12.5 (DAB counterstained by hematoxylin). The red arrow indicates the cell layer above the proliferating (BrdU positive) cells. The yellow lines illustrate the columnar arrangement of cells and the trend of radial migration. Control: *Pdss2$^{f/+}$* (E), mutant: *Pdss2$^{f/-}$; Pax2-cre* (F). **G-H:** BrdU assay of cerebellum at E14.5. Control: *Pdss2$^{f/+}$* (G), mutant: *Pdss2$^{f/-}$; Pax2-cre* (H). Panels (A-H) are representative images of 4 control and 4 mutant mice at both E12.5 and E14.5. **I-J:** Immunostaing of nestin for radial glial cells at E12.5 (DAB). Control: *Pdss2$^{f/+}$* (I), mutant: *Pdss2$^{f/-}$; Pax2-cre* (J). **I'-J':** Magnifications of squared areas in I and J, respectively. The contour of mutant cerebellum is outlined by yellow dashed lines in J and J'. **K-L:** Immunostaining of Tuj1 (neuronal Class III β-tubulin) at E14.5 (DAB counter stained by hematoxylin). Control: *Pdss2$^{f/+}$* (K), mutant: *Pdss2$^{f/-}$; Pax2-cre* (L). The red arrow indicates the thickness of Tuj1 negative cell layer. Panels (I-J') are representatives of 3 control and 3 mutant mice. **M:** Overall cell density in the

cerebellum of control (*Pdss2*$^{f/+}$ or *Pdss2*$^{f/+}$*; Pax2-cre*) and mutant (*Pdss2*$^{f/-}$*; Pax2-cre*) embryos at E12.5 and E14.5. At E12.5, the overall cell density of control group (0.0258, ± 0.00116 cells/μm^2, n = 3) shows no significant difference from that of mutant group (0.0262, ± 0.000823 cells/μm^2, n = 4) by independent t test (p = 0.776, not labeled). Error bars represent ± SD (0.00202 for control and 0.00165 for mutant). At E14.5, the overall cell density of control group (0.0127, ± 0.000593 cells/μm^2, n = 4) is significantly lower than that of mutant group (0.0200, ± 0.000868 cells/μm^2, n = 4) by independent t test (p < 0.001). Error bars represent ± SD (0.00119 for control and 0.00174 for mutant). **N:** BrdU index in the cerebellum of control (*Pdss2*$^{f/+}$ or *Pdss2*$^{f/+}$*; Pax2-cre*) and mutant (*Pdss2*$^{f/-}$*; Pax2-cre*) embryos at E12.5 and E14.5. At E12.5, the BrdU index of control group (23.09%, ± 0.00806, n = 3) has no significant difference from that of mutant group (20.37%, ± 0.0142, n = 4) by independent t test (p = 0.193, not labeled). Error bars represent ± SD (0.0140 for control and 0.02840 for mutant). At E14.5, the BrdU index of control group (8.408%, ± 0.00436, n = 4) is very similar to that of mutant group (8.048%, ± 0.00594, n = 4) by independent t test (p = 0.642, not labeled). The calculations for panels M-N are detailed in *Materials and methods*. Scale bars: 150 μm in (A-D) and (G-H); 75 μm in (E-F), (I-J), (K-L); 25 μm in (I'-J').

Fig. 5: The progression of cerebellum hypoplasia since E14.5. **A-B:** TUNEL assay of cerebellum coronal section at E14.5 (DAB counter stained by hematoxylin). Control: *Pdss2*$^{f/+}$ (A), mutant: *Pdss2*$^{f/-}$*; Pax2-cre* (B). **C:** Percentage of apoptotic cells in total cells in the cerebellum of control (*Pdss2*$^{f/+}$ or *Pdss2*$^{f/+}$*; Pax2-cre*) and mutant (*Pdss2*$^{f/-}$*; Pax2-cre*) embryos at E14.5. The percentage of apoptotic cells in mutant group (0.931%, ± 0.000311, n

= 3) is significantly higher than that of control group (0.158%, ± 0.000242, n = 3) by independent t test ($p < 0.001$). Error bars represent ± SD (0.000538 for control and 0.000419 for mutant). Calculation method is detailed in *Materials and methods*. **D-E:** TUNEL assay of cerebellum coronal section at E15.5 (DAB counter stained by hematoxylin). Control: *Pdss2*$^{f/+}$ (D), mutant: *Pdss2*$^{f/-}$*; Pax2-cre* (E). **F-G:** TUNEL assay of cerebellum coronal section at E16.5 (DAB counter stained by hematoxylin). Control: *Pdss2*$^{f/+}$ (F), mutant: *Pdss2*$^{f/-}$*; Pax2-cre* (G). **E' and G':** Magnifications of squared areas in E and G, respectively. **H-I:** BrdU assay (DAB) on coronal sections of cerebellum pre-stained by whole mount X-gal staining at E17.5. Control: *Pdss2*$^{f/+}$*; ROSA26*$^{lacZ/+}$*; Pax2-cre* (H), mutant: *Pdss2*$^{f/-}$*; ROSA26*$^{lacZ/+}$*; Pax2-cre* (I). **I':** A magnification of the squared area in I. **J-K:** TUNEL assay (FITC, green) co-stained for β-galactosidase (Cy3, red) on coronal cerebellum section at E18.5. Counter stained with DAPI (blue). Control: *Pdss2*$^{f/+}$*; ROSA26*$^{lacz/+}$ (J), mutant: *Pdss2*$^{f/-}$*; ROSA26*$^{lacZ/+}$*; Pax2-cre* (K). **K':** A magnification of the squared area in K (the channel for DAPI is removed). The insert at the upper right is a close-up view of the squared area, and apoptotic bodies are indicated by yellow arrows. Scale bars: 150 μm in (A-B, D-E, F-G, H-I, J-K); 75 μm in (E'), (G'), (I'); 50 μm in (K').

Fig. 6: Whole mount *Fgf8 in situ* hybridization (back view from the dorsal side). The yellow arrow in each panel indicates *Fgf8* expression at isthmus. Scale bar: 0.2 mm.

Fig. 7: Abnormal mitochondria and autophagic-like vacuoles in mutant cerebellum cells at E18.5. Coronal sections of cerebellum were examined by transmission electron microscopy.

A: A normal cell in *Pdss2*$^{f/+}$ (control) cerebellum (Nu: nucleus). **B:** Normal mitochondria (M, pointed by yellow arrows) in *Pdss2*$^{f/+}$ cerebellum. **C:** An apoptotic cell in *Pdss2*$^{f/-}$*; Pax2-cre* (mutant) cerebellum. **D:** Abnormal mitochondria (M*, pointed by yellow arrows) in *Pdss2*$^{f/-}$*; Pax2-cre* cerebellum. Lys: lysosome. **E-G:** Autophagic-like structures in cells of *Pdss2*$^{f/-}$*; Pax2-cre* cerebellum. A defective mitochondrion is engulfed by rER, indicated by yellow arrows (E). Residual bodies (R), indicated by yellow arrows (F). A magnification of the residual bodies (R) in a lysosome (Lys) (G). **H:** Comparison between the percentage of cells with autophagic-like morphology in *Pdss2*$^{f/+}$ and *Pdss2*$^{f/-}$*; Pax2-cre* cerebellum (4 randomly picked areas for each). Mean of control = 11.91% (SEM = 0.00874), mean of mutant = 30.90% (SEM = 0.00615). Error bars represent ± SD (0.0175 for control and 0.0123 for mutant). $p < 0.001$ by independent t-test. Detailed calculation is given in *Materials and methods*. Scale bars: 2 μm in (A) and (C); 0.2 μm in (B) and (G); 0.5 μm in (D-F).

Fig. 8: Foot print analysis of aged *Pdss2*$^{f/-}$*; Pcp2-cre* mouse at 1 year old. **A:** A representative walking path of control mouse (*Pdss2*$^{f/+}$*; Pcp2-cre*). **B:** An example of walking path of mutant mouse (*Pdss2*$^{f/-}$*; Pcp2-cre*) with two additional steps indicated by gray arrow heads. **C:** An example of mutant foot print demonstrating that the mouse slides to the left during walking. The long gray arrow shows the direct of sliding between two adjacent steps. Panels A-C are representative pictures from 4 mutant mice (*Pdss2*$^{f/+}$*; Pcp2-cre*) and 4 control littermates (*Pdss2*$^{f/-}$*; Pcp2-cre*). **D:** Percentage of walking with additional steps. The mutant group (16.15%, ± 0.04288, n = 4) shows a significantly higher frequency of demonstrating additional steps during walking than the control group (8.576%, ± 0.06865, n = 4) by ANOVA ($p = 0.018$). The error bars represent ± SD (0.08576 for control and 0.13729 for mutant). **E:**

Mean stride length. The measurements of stride length on the left and right side is pooled because side does not has a significant effect on the stride length ($p = 0.786$ by ANOVA). The mean stride length of mutant group (4.1, ± 0.2 cm, n = 4) is significantly shorter than that of control group (6.7, ± 0.3 cm, n =4) by ANOVA ($p < 0.001$). Detailed method of calculation is given in *Materials and methods*.

Fig. 9: Progressive loss of cerebellum Purkinje cells in adult *Pdss2$^{f/-}$; Pcp2-cre* mouse. **A and D:** Whole mount X-gal staining of cerebellum of *Pdss2$^{f/+}$; ROSA26$^{lacZ/+}$; Pcp2-cre* mouse (B) and *Pdss2$^{f/-}$; ROSA26$^{lacZ/+}$; Pcp2-cre* mouse (E) cerebellum at 1 month old. **B-E:** Para-sagittal section of X-gal stained cerebellum shown in A and D, respectively. **C and F:** Immunostaining of CALB-28K for Purkinje cells in *Pdss2$^{f/+}$; ROSA26$^{lacZ/+}$; Pcp2-cre* mouse (C) and *Pdss2$^{f/-}$; ROSA26$^{lacZ/+}$; Pcp2-cre* mouse (F) at 1 month old (para-sagittal section, DAB counterstained by hematoxylin). **G and J:** Whole mount X-gal staining of cerebellum of *Pdss2$^{f/+}$; ROSA26$^{lacZ/+}$; Pcp2-cre* mouse (G) and *Pdss2$^{f/-}$; ROSA26$^{lacZ/+}$; Pcp2-cre* mouse (J) cerebellum at 6 months. **H and K:** Para-sagittal section of X-gal stained cerebellum shown in G and J, respectively. **I and L:** Immunostaining of CALB-28K for Purkinje cells in *Pdss2$^{f/+}$; ROSA26$^{lacZ/+}$; Pcp2-cre* mouse (I) and *Pdss2f/-; ROSA26lacZ/+; Pcp2-cre* mouse (L) at 6 months (para-sagittal section, DAB counterstained by hematoxylin). All panels are representatives of 3 mice. Scale bar: 1 mm in (A), (D), (G), and (J). 75 μm for all other panels.

Fig. 10: Increased apoptosis in aged *Pdss2$^{f/-}$; Pcp2-cre* mouse cerebellum. **A-D:** TUNEL assay (FITC) of *Pdss2$^{f/+}$* mouse cerebellum (A-B) and *Pdss2$^{f/-}$; Pcp2-cre* mouse cerebellum

(C-D) at 6 months. Nucleus counter stained with DAPI. **E-H:** TUNEL assay (FITC) of *Pdss2*$^{f/+}$ mouse cerebellum (A-B) and *Pdss2*$^{f/-}$*; Pcp2-cre* mouse cerebellum (C-D) at 9.5 months. Nucleus counter stained with DAPI. Panels (A-H) are representatives of 3 mice with the same genotype. **I-L:** Ultra-structure of *Pdss2*$^{f/+}$ and *Pdss2*$^{f/-}$*; Pcp2-cre* mouse cerebellum at 8 months. A representative apoptotic cell in mutant cerebellum (J) is compared with a normal cell in control cerebellum (I). Nu = nucleus. An example of swollen mitochondria in mutant cerebellum (L) is compared with normal mitochondria in control cerebellum (K). Scale bar: 150 μm in (A), (C), (E), (G); 75 μm in (B), (D), (F), (H); 2 μm in (I); 1 μm in (J); 0.2 μm in (K); 0.5 μm in (L).

Video. 1: *Pdss2*$^{f/+}$*; ROSA26*$^{lacZ/+}$*; Pcp2-cre* mouse at 4.5 months. The control mouse can walk normally on the bench and stand with its hind-limbs against the rim of the tray.

Video. 2: *Pdss2*$^{f/-}$*; ROSA26*$^{lacZ/+}$*; Pcp2-cre* mouse at 4.5 months. The mutant mouse can also walk normally on the bench and stand with its hind-limbs against the rim of the tray as the control littermate shown in Video. 1.

Video. 3: *Pdss2*$^{f/+}$*; ROSA26*$^{lacZ/+}$*; Pcp2-cre* mouse at 9.5 months. The control mouse can walk normally on the bench and is also capable of standing with its hind-limb against the rim of both low-edged plastic tray and high-edged paper box, just like those mice shown in Video. 1 and 2. In addition, the mouse can maintain its balance and continuously walk on a rod.

Video. 4: *Pdss2*$^{f/-;}$ *ROSA26*$^{lacZ/+}$*; Pcp2-cre* mouse at 9.5 months. The mutant mouse demonstrates defects in movement coordination when walking on the bench and fails to stand with its hind-limbs in either low-edged or high edged container. Furthermore, the mouse cannot maintain its balance on the rod. It frequently slips and eventually falls off.

Figure-1

Click here to download high resolution image

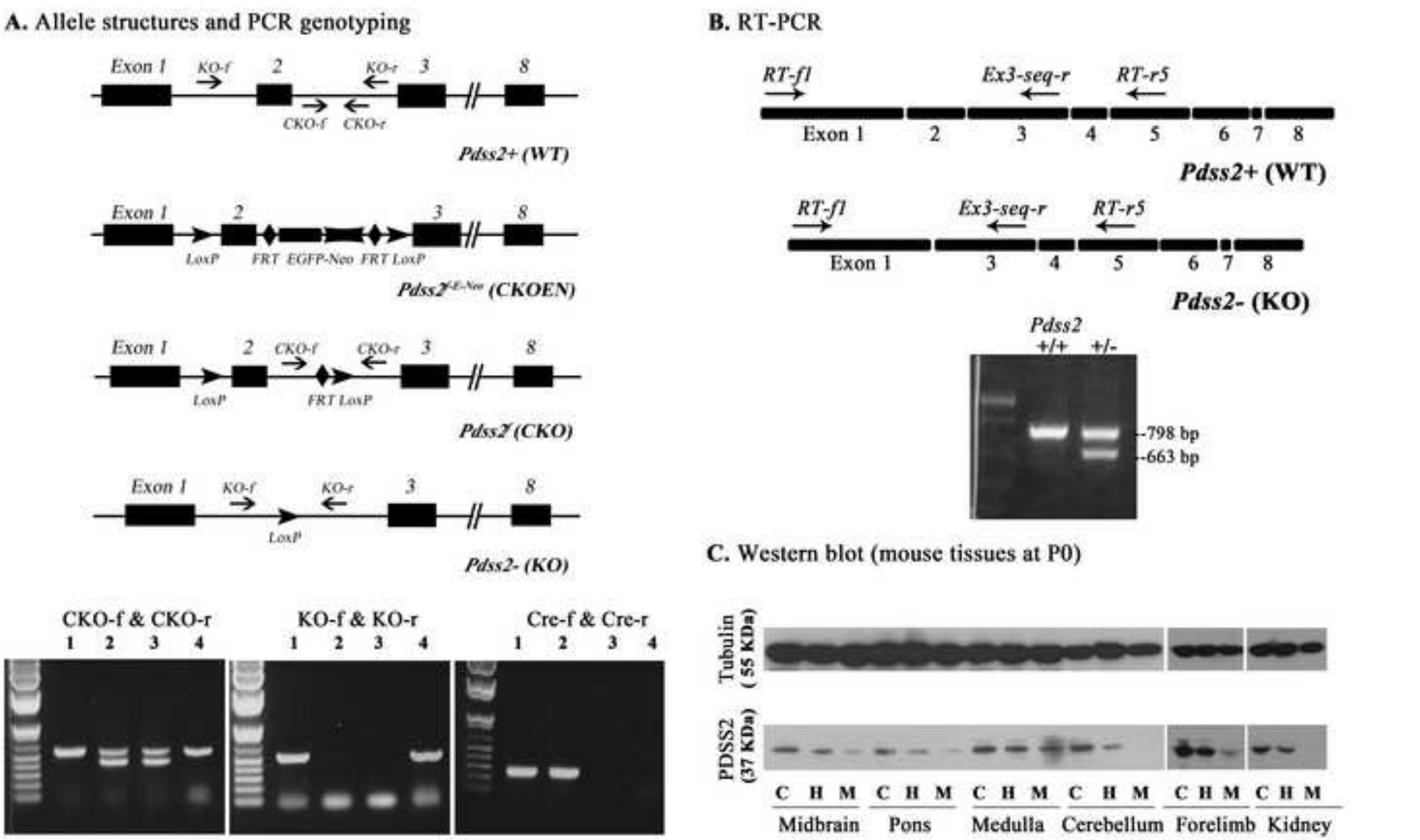

Figure-2

Click here to download high resolution image

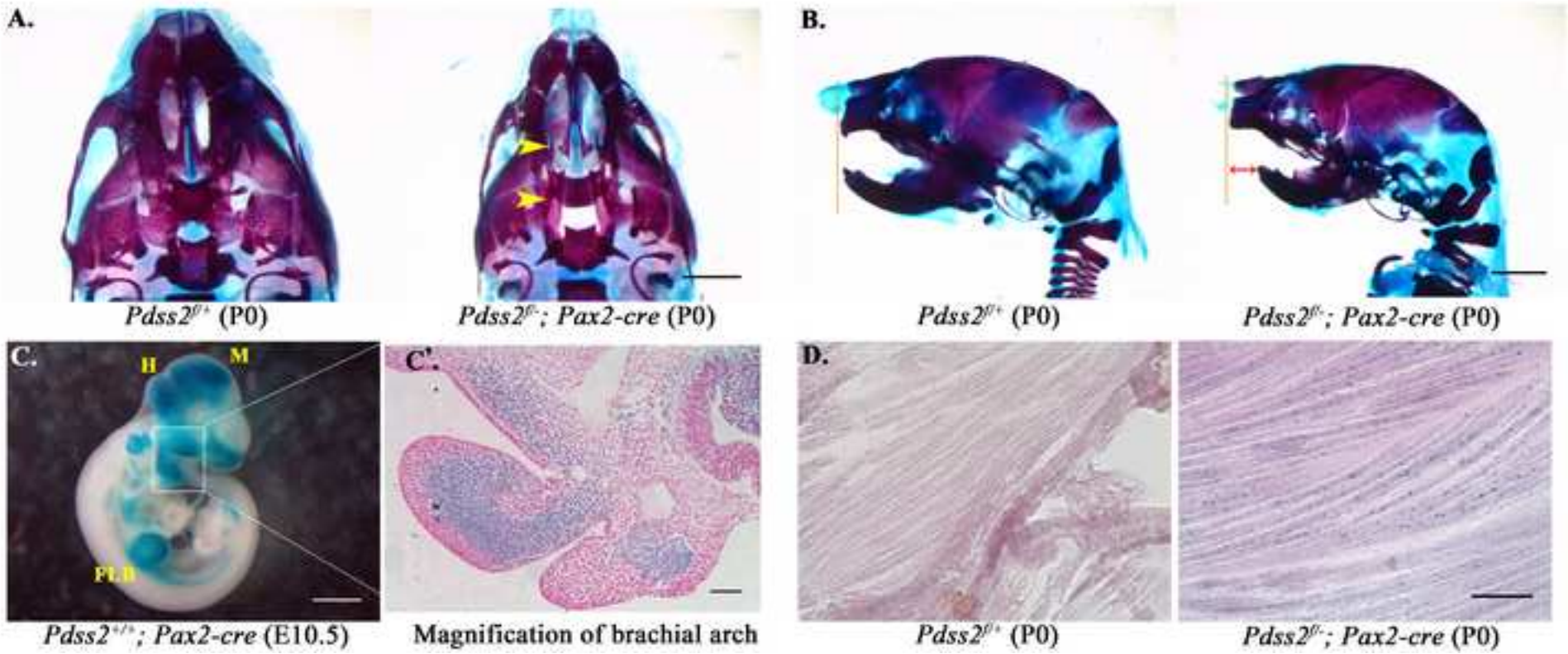

Figure-3

Click here to download high resolution image

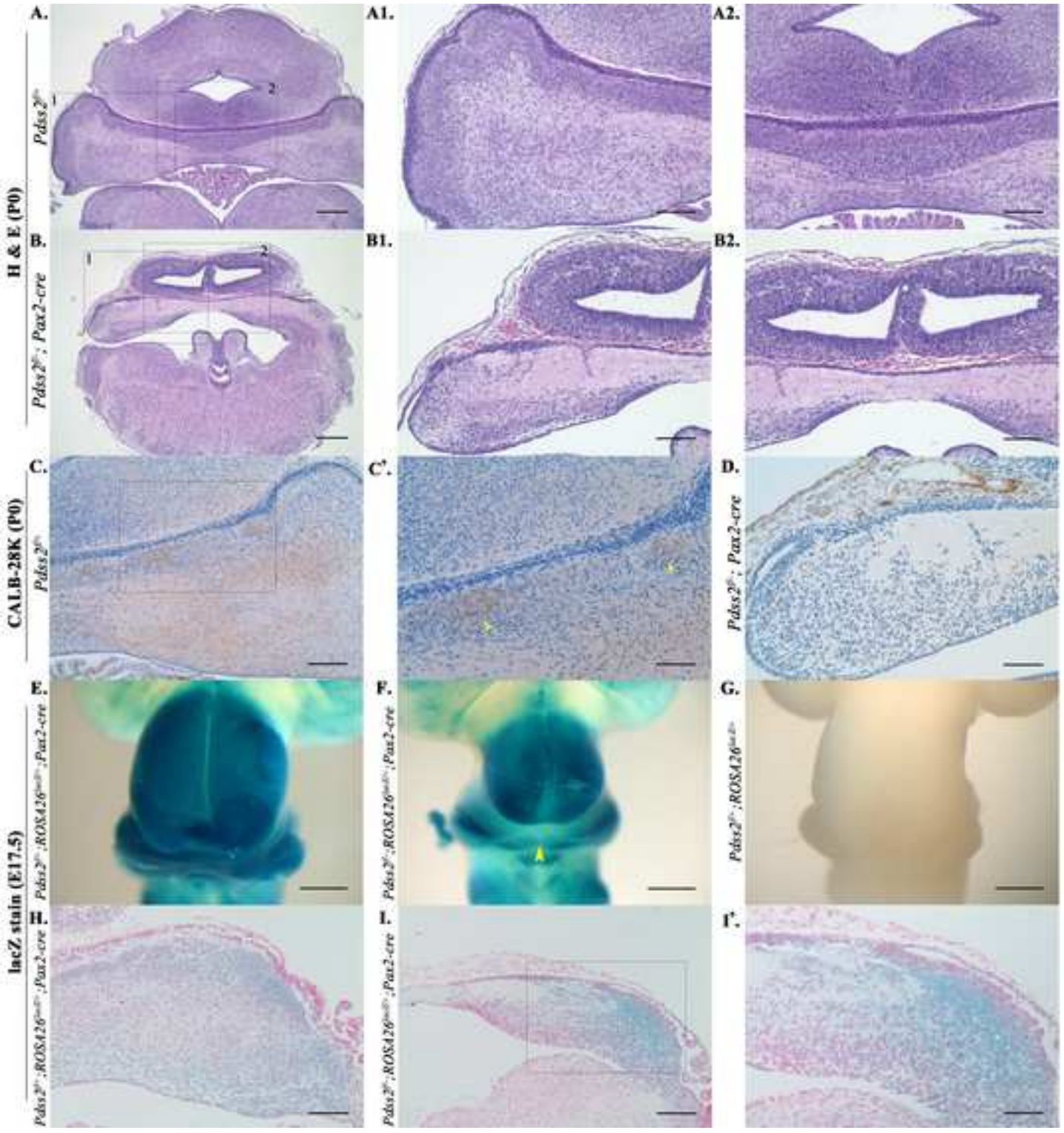

Figure-4

Click here to download high resolution image

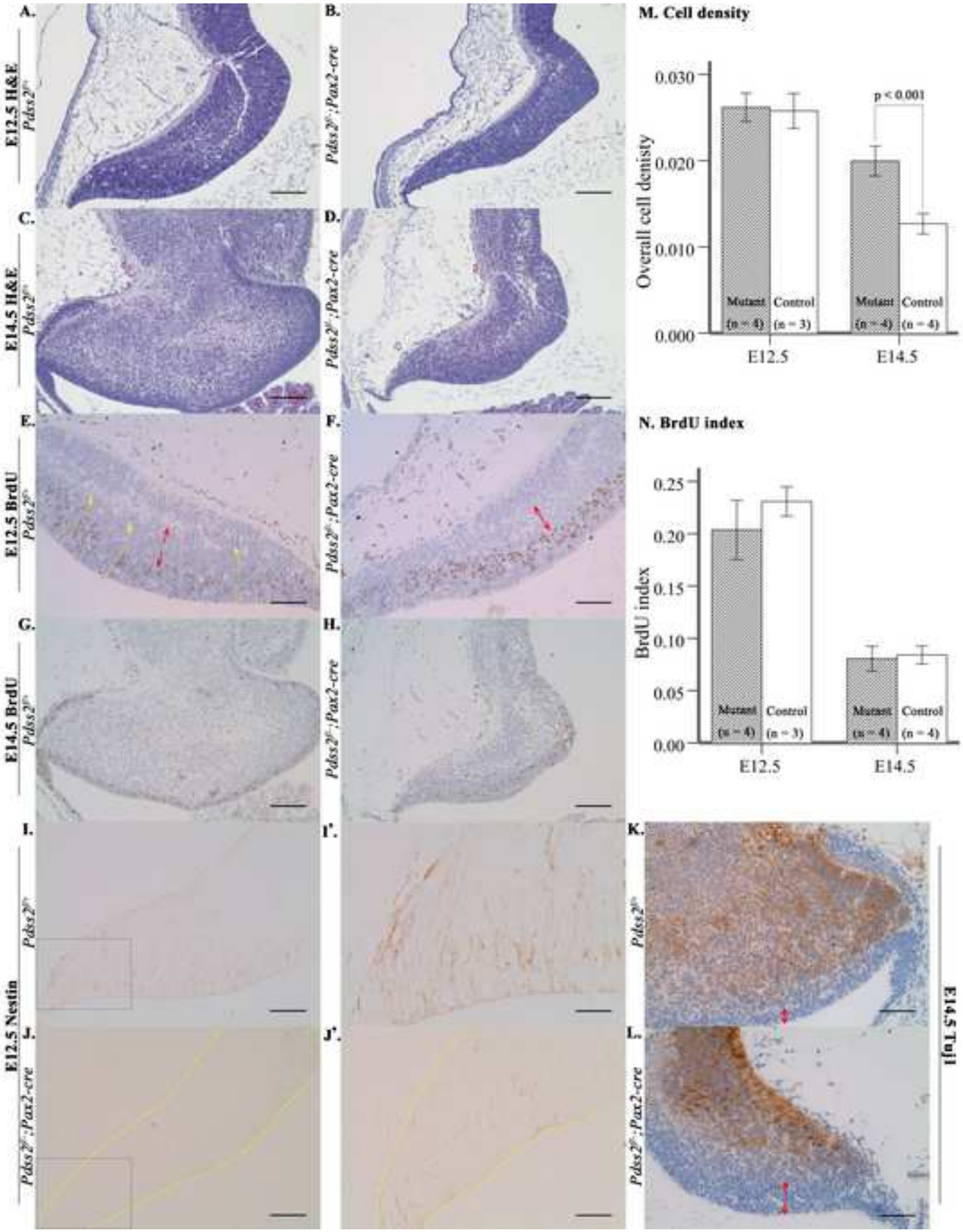

Figure-6

Click here to download high resolution image

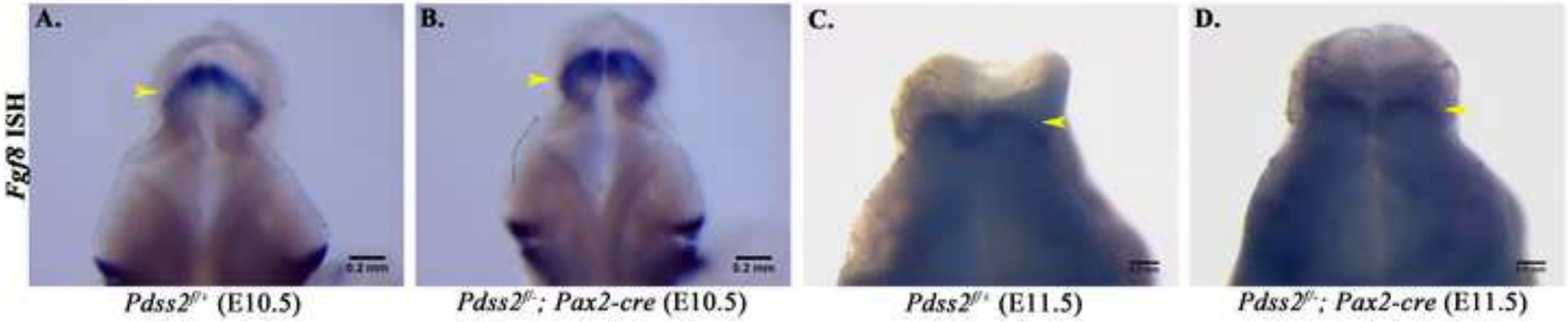

Figure-5

Click here to download high resolution image

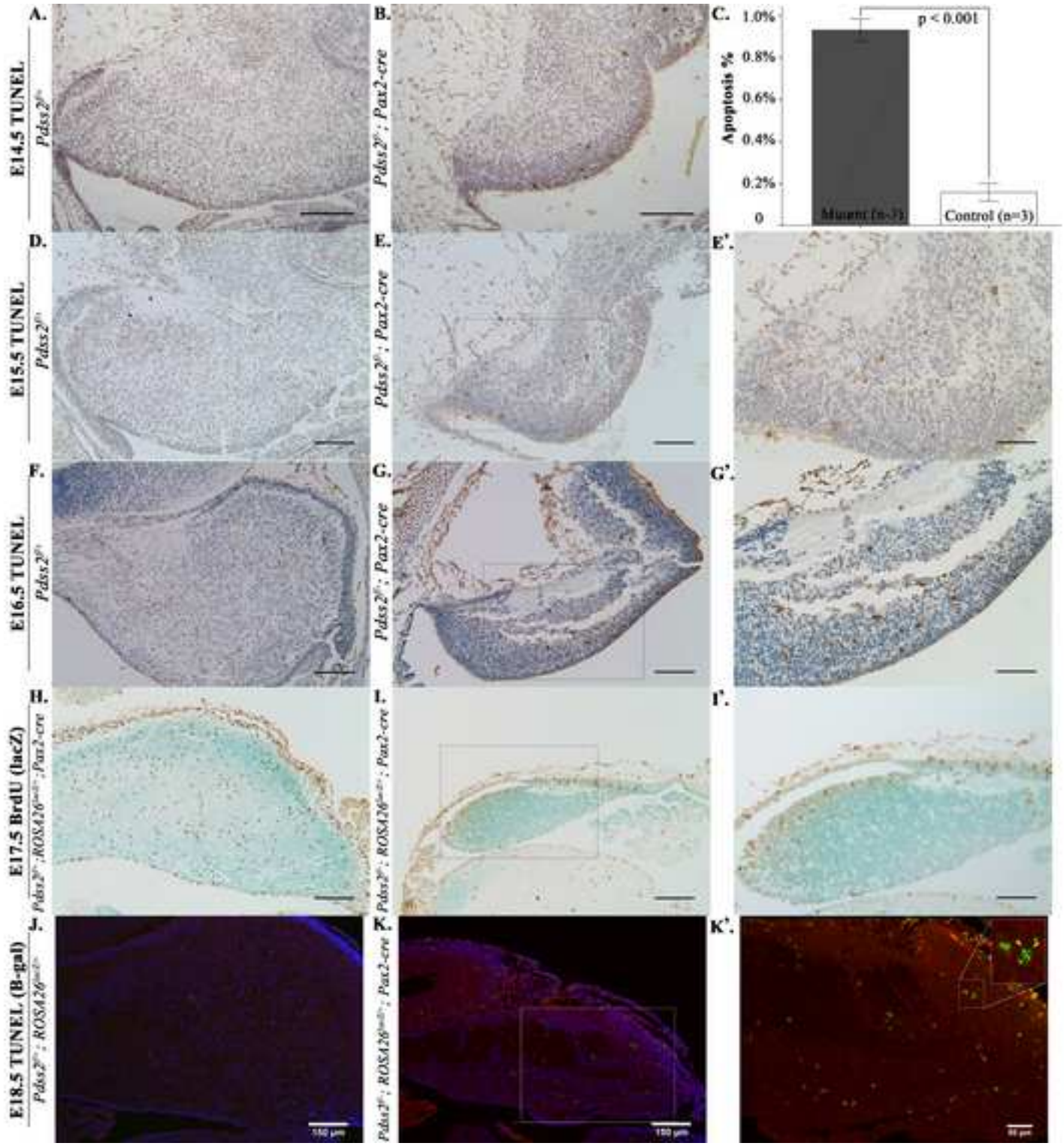

Figure-7

Click here to download high resolution image

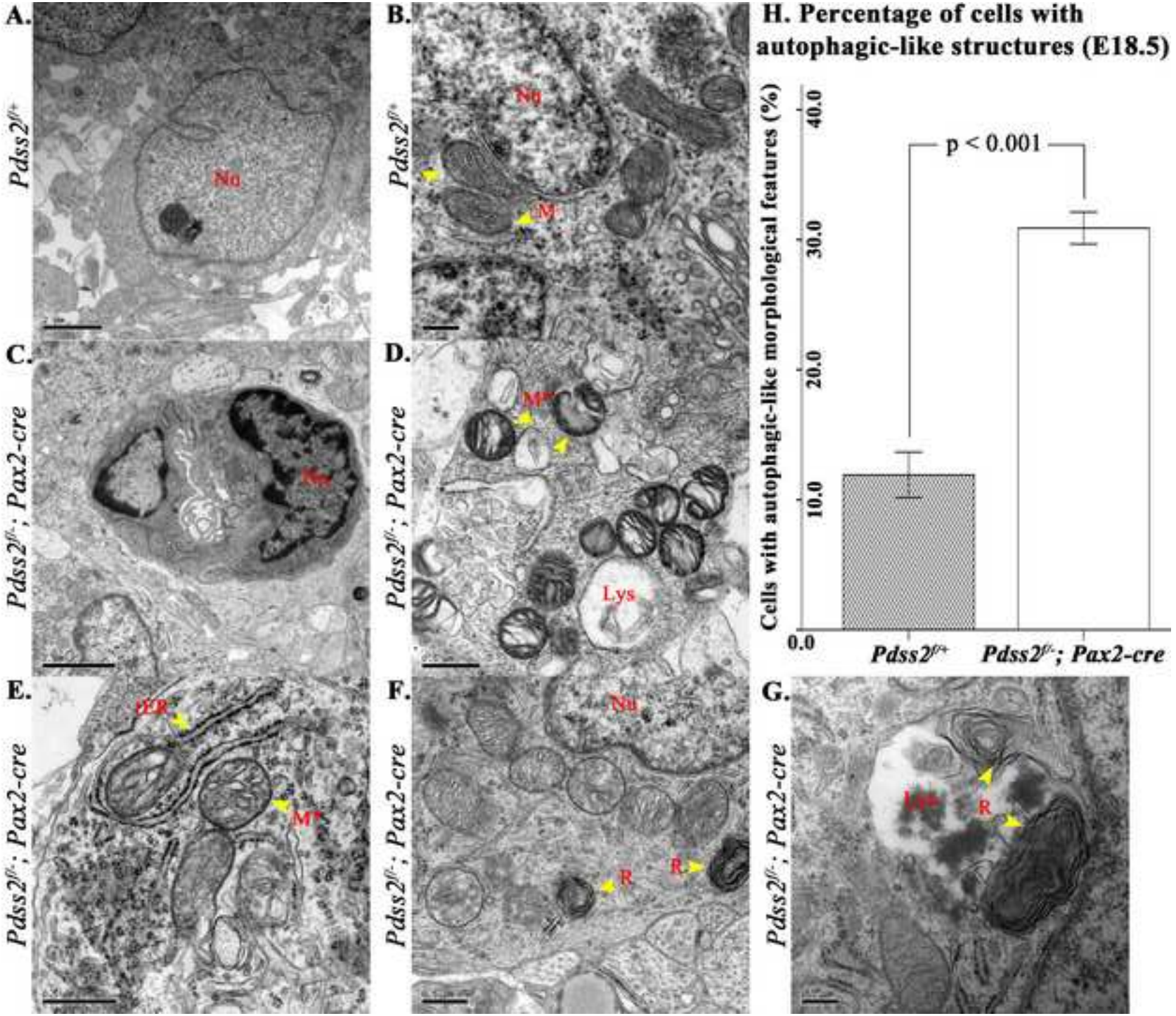

Figure-8

Click here to download high resolution image

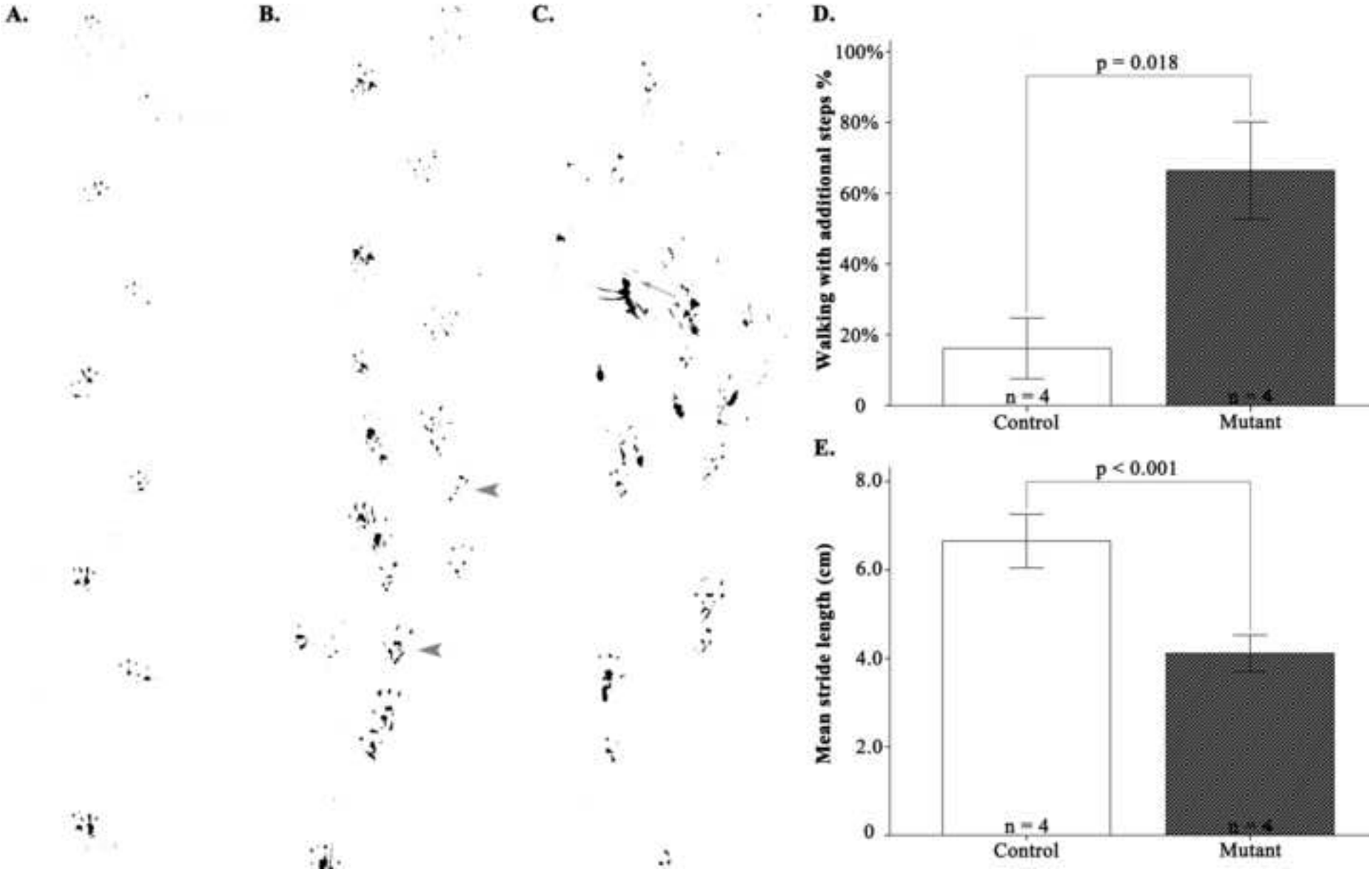

Figure-9

Click here to download high resolution image

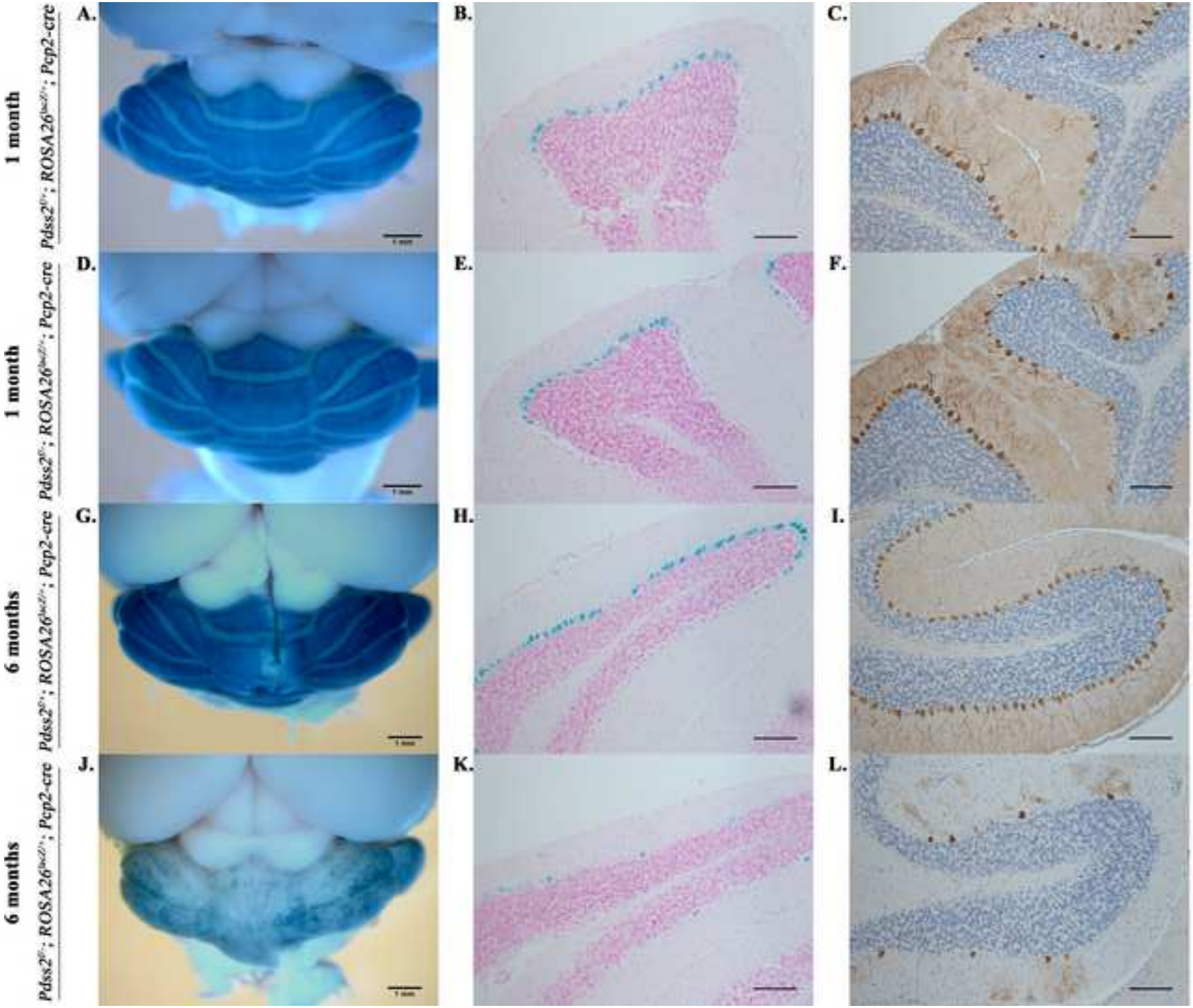

Figure-10

Click here to download high resolution image

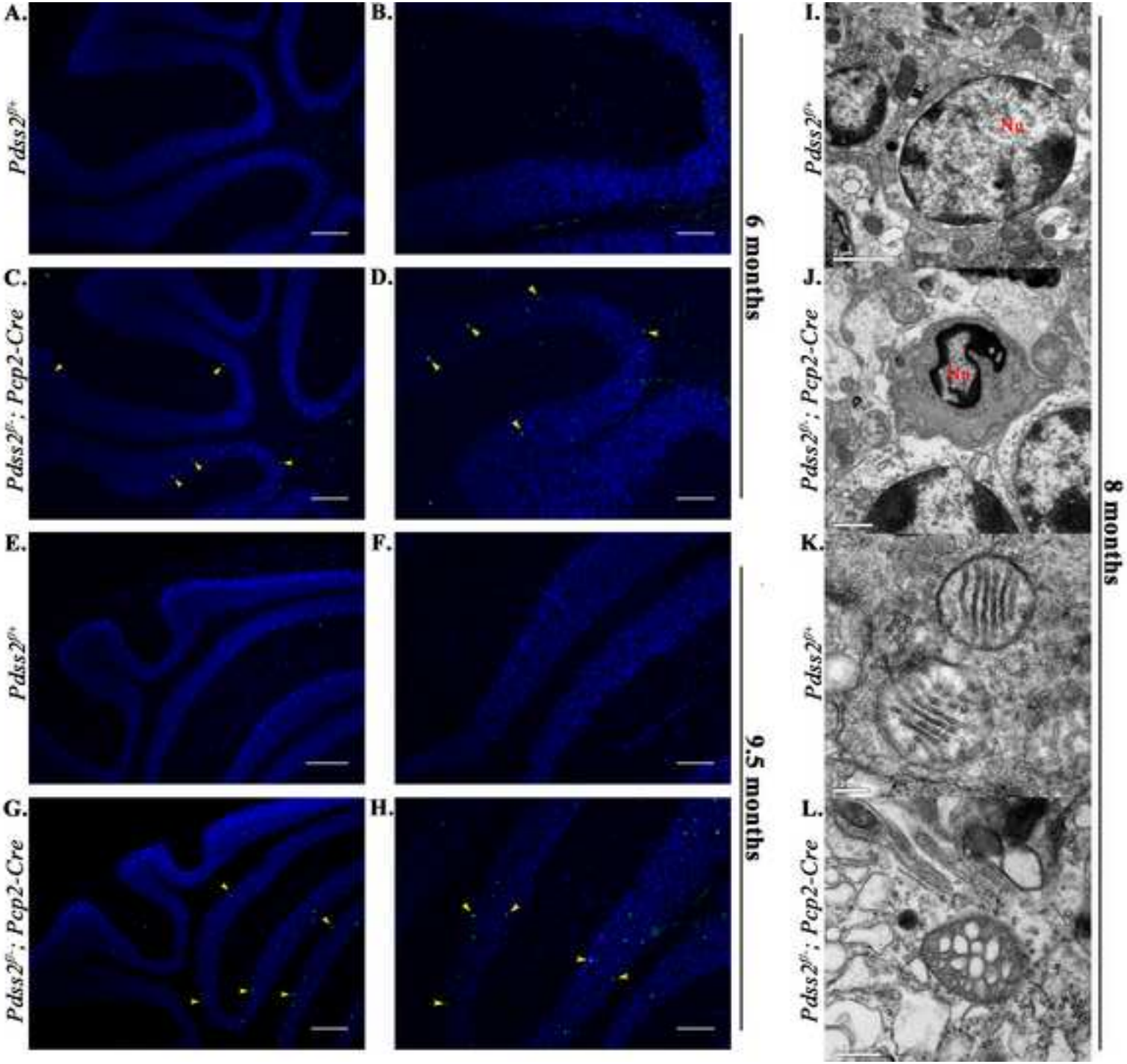

Table 1: Genotyping primers and amplification conditions

Mouse	Primers (5'-3')	PCR conditions	Alleles	Product (bp)
Pdss2$^{f/+}$	CKO-f: TAGTCCTTTGTGAGTTACCCGTTGG	Routine[a], Ta 56℃	*Pdss2*$^{+}$	422
	CKO-r: GCCATTCACTTTCCACTGTCACC		*Pdss2*^{f}	584
Pdss2$^{+/-}$	KO-f: GGGGAGTTATCATATCCGTTTATC	Routine, Ta 58℃	*Pdss2*$^{+}$	2,143
	KO-r: GGGCAGGCTCAAAGTCAGGAAG		*Pdss2*$^{-}$	522
Pax2-cre	Cre-f: GGACATGTTCAGGGATCGCCAGGCG	Routine, Ta 58℃	*Pax2-cre*	270
	Cre-r: GCATAACCAGTGAAACAGCATTGCTG			
ROSA26$^{lacZ/+}$	ROSA883(f): AAGTCGCTCTGAGTTGTTAT	Routine, Ta 59℃	*ROSA26*$^{+}$	550
	ROSA2(r): GCGAAGAGTTTGTCCTCAACC	Primer ratio[b]	*ROSA26*^{lacZ}	300
	ROSA3(r): GGAGCGGGAGAAATGGATATG			

a: Routine PCR program: 95℃, 5 min. 95℃, 30 sec; Ta (as specified), 30 sec; 72℃, 45 sec, for 35 cycles. 72℃, 10 min.

b: Primer ratio: three primers ROSA883:ROSA2:ROSA3 = 2:1:2 (molar ratio).

Supplementary main text

Click here to download Supplementary Material: Supplementary data.doc

Supplementary Table-1

Click here to download Supplementary Material: Table S1.doc

Supplementary Figure-1

Click here to download Supplementary Material: Fig-S1.tif

Supplementary Figure-2

Click here to download Supplementary Material: Fig-S2.tif

Supplementary Figure-4

Click here to download Supplementary Material: Fig-S4.tif

Supplementary Figure-3

Click here to download Supplementary Material: Fig-S3.tif

Video-1

Click here to download Supplementary Material: Video. 1.mp4

Video-2

Click here to download Supplementary Material: Video. 2.mp4

Video-3

Click here to download Supplementary Material: Video. 3.mp4

Video-4

Click here to download Supplementary Material: Video. 4.mp4